HAL open science

Calibration of short-wave infraRed (SWIR) hyperspectral imaging using diffuse reflectance infrared Fourier transform spectroscopy (DRIFTS) to obtain continuous logging of mineral abundances along sediment cores

Stoil Chapkanski, Kevin Jacq, Gilles Brocard, Cécile Vittori, Maxime Debret, Andrea U De Giorgi, Daniele d'Ottavio, Enrico Maria Giuffré, Jean-Philippe Goiran

To cite this version:

Stoil Chapkanski, Kevin Jacq, Gilles Brocard, Cécile Vittori, Maxime Debret, et al.. Calibration of short-wave infraRed (SWIR) hyperspectral imaging using diffuse reflectance infrared Fourier transform spectroscopy (DRIFTS) to obtain continuous logging of mineral abundances along sediment cores. Sedimentary Geology, 2022, 428, pp.106062. 10.1016/j.sedgeo.2021.106062 . hal-03505951

HAL Id: hal-03505951

https://hal.science/hal-03505951v1

Submitted on 8 Jan 2024

HAL is a multi-disciplinary open access archive for the deposit and dissemination of scientific research documents, whether they are published or not. The documents may come from teaching and research institutions in France or abroad, or from public or private research centers.

L'archive ouverte pluridisciplinaire **HAL**, est destinée au dépôt et à la diffusion de documents scientifiques de niveau recherche, publiés ou non, émanant des établissements d'enseignement et de recherche français ou étrangers, des laboratoires publics ou privés.

Distributed under a Creative Commons Attribution - NonCommercial 4.0 International License

Version of Record: https://www.sciencedirect.com/science/article/pii/S0037073821002141
Manuscript_48b4f712b606e6013759363548be5088

Calibration of Short-Wave InfraRed (SWIR) hyperspectral imaging using Diffuse Reflectance Infrared Fourier Transform spectroscopy (DRIFTS) to obtain continuous logging of mineral abundances along sediment cores

Chapkanski Stoil[1,2], Jacq Kévin[3], Brocard Gilles[1], Vittori Cécile[1,4], Debret Maxime[3], De Giorgi Andrea U., D'Ottavio Daniele[7], Giuffré Enrico Maria[8], Goiran Jean-Philippe[1]

[1]Archéorient, UMR 5133, University of Lyon 2-CNRS, 7 rue Raulin, 69007 Lyon, France.

[2]Laboratory of Physical Geography (LGP), UMR 8591, University Paris 1, Panthéon-Sorbonne – CNRS,1 place Aristide Briand, 92195 Paris, France.

[3]Normandie Univ, UNIROUEN, UNICAEN, CNRS, M2C, 76000 Rouen, France

[4]Laboratoire Image Ville Environnement (LIVE), UMR 7362, University of Strasbourg, Faculty of Geography and Urban planning, 3 rue de l'Argonne, 67083 Strasbourg, France

[5]Florida State University, Department of Classics, 324 Dodd Hall, Tallahassee, FL, 32306-1510, United States of America;

[6]Freie Universität, Insitut für Klassische Archäologie, Fabeckstraße 23-25, Berlin, 14195, Germany

[7]Unigeo S.r.l., Via Idrovore della Magliana, n. 147, Rome, Italia

[8]Soprintendenza Archeologia Belle Arti e Paesaggio per le Province di Siena, Grosseto e Arezzo, Siena, Italia

Corresponding author

Stoil Chapkanski

Laboratory of Physical Geography,

UMR 8591, Université Paris 1 Panthéon-Sorbonne - CNRS,

1 place Aristide Briand, 92195, Paris, France.

stoil.chapkanski@protonmail.com

+33 1 45 07 55 83

© 2021 published by Elsevier. This manuscript is made available under the CC BY NC user license
https://creativecommons.org/licenses/by-nc/4.0/

Abstract

Sediment cores are a major source of sub-surface data for a variety of environmental research endeavors, as well as mining and civil engineering applications. In paleo-environmental studies, fluctuations in mineral abundances along sediment cores are used to study climate change, sea-level variations, sediment dynamics, and landscape evolution. Increasing reliance on such proxies spurs the need for reliable and time-saving analytical tools and procedures. Diffuse Reflectance Infrared Fourier Transform spectroscopy (DRIFTS) is a rapid, non-destructive and accurate tool for quantification of mineral abundances. We use DRIFTS to calibrate Short-Wave InfraRed (SWIR) hyperspectral images (HSI) of a sediment core, in order to convert point-specific DRIFTS measurement of mineral abundances into a continuous record of mineral abundances along the core. Initially, single-phase and mineral assemblages of quartz, calcite, and clay mineral are created and measured by DRIFTS to establish calibration curves to convert DRIFTS data into mineral abundances, as $\%_{wt}$ of bulk sediment samples. Mineral abundances are then measured by DRIFTS in a set of 60 samples from a core drilled into the Albegna River delta, Tuscany, Italy in the Fall of 2020. SWIR-HSI of the core are then obtained and averaged over the areas corresponding to the samples taken for point-specific DRIFTS measurements. Least squares regressions are established between SWIR-HSI and DRIFTS data over these areas. This calibration is then used to convert SWIR-HSI of the entire core into a continuous prediction of quartz, calcite, and clay minerals abundances along the core. The continuous record highlights sharp changes in mineral composition, smeared out in the discontinuous DRIFTS record. The advantages and limitations of the method, as well as its applicability to other sedimentary environments are discussed.

Keywords: Infrared spectroscopy, hyperspectral imaging, sediment core, chemometrics, minerals, high resolution analysis

1. Introduction

Sediment cores are a major source of sub-surface information in stratigraphic and paleo-environmental studies. They are used to reconstruct past- climate (Miller et al., 2020), sea-levels (Kelsey et al., 2015), landscapes (Pennington et al., 2017) archeological environments (Delile et al., 2018; Salomon et al., 2018); for technical essays in mining and civil engineering (Kahraman et al., 2016), and for the assessment of natural (Grand Pre et al., 2012) and anthropogenic (Bigus et al., 2014) hazards. Variations of geochemical and mineralogical abundances along sediment cores are used as proxies for fluctuations of past climates (Solotchina et al., 2009; Wan et al., 2007; Tamburini et al., 2003), fluctuations in weathering rate, sedimentation rate, and shifts in depositional patterns (He et al., 2020; Wang et al., 2016; Hamdan et al., 2018; Lupker et al., 2012; Garzanti et al., 2010; 2011; Martinelli et al., 1993). They are used to assess sediment provenance and thereby track landscape evolution (Li et al., 2014; Andrews and Eberl, 2012; Liu et al., 2020; Pe-Piper et al., 2016; Heroy et al., 2003; Wahab and Stanley, 1991). Geochemical and mineralogical quantitative analyses traditionally resort to precise but time-consuming and expensive analytical methods, such as atomic absorption spectroscopy - AAS, inductive coupled plasma mass spectroscopy – ICP-MS (Willis, 1986), Scanning electron microscopy - SEM (Schulz et al., 2020), X-Ray diffraction - XRD (Moore and Robert, 1997) and Raman spectroscopy (Larkin, 2011). The accelerating growth of sediment core libraries worldwide has motivated the use of faster and less costly analytical approaches, such as portable X-ray fluorescence - PXRF (Duee et al., 2019), Attenuated Total Reflectance Fourier Transform Infrared spectroscopy - ATR-FTIRS (Milosevic, 2012), and Diffuse Reflectance Infrared Fourier Transform spectroscopy - DRIFTS (Frei and MacNeil, 2018). In the meantime, the need for high-resolution information on finely laminated sediments spurred the adaptation of non-destructive scanning and imaging techniques to sediment cores (Rothwell and Rack, 2006), most notably XRF core scanning (Davies et al., 2015), X-Ray tomography (Zonta et al., 2021; Paris et al., 2020), and hyperspectral imaging - HSI (Jacq et al., 2019a, b). Pioneering HSI on soils (Zaeem et al., 2021) and lake sediments (Makri et al., 2020; Rapuc et al., 2020; Ghanbari et al., 2020; Jacq et al., 2019a, b; Van Exem et al., 2018; Rivard et al., 2018; Butz et al., 2017; Aymerich et al., 2016) yields encouraging results. So far, HSI has been applied to organic-rich and silty-clayey lacustrine sediments and to nonwater-saturated sedimentary rocks with fairly homogenous grain size distribution

along core. The conversion of HSI data into chemical and mineral abundances requires calibration against standard analytical methods such as ICP-MS (Zaeem et al., 2021; Rivard et al., 2018), Loss on Ignition – LOI (Jacq et al., 2019b), particle size distribution – PSD (Jacq et al., 2019), and XRD (Greene et al., 2019).

FTIRS has been used for five decades (Srodo, 2002) to determine the abundance of carbonates (So et al., 2020; Henry et al., 2017), clay minerals (Srodo, 2002; Joussein et al., 2001), amorphous silica and quartz (Bertaux et al., 1998, Bandopadhyay, 2010; Melucci et al., 2019), other tectosilicates and sulfates (Muller et al., 2014; Bosch-Reig et al., 2017; Painter et al., 1978), total organic carbon (Vogel et al., 2008; Rosen et al., 2010; 2011; Hahn et al., 2011), metals (Moros et al., 2009; Siebielec et al., 2004), and plastic microparticles (Hahn et al., 2019).

We used DRIFTS to analyze the evolution of the provenance of sediments deposited during the Holocene in the delta of the Albegna River, in Tuscany, Italy, starting with a 14 m-long core obtained in 2020 (sediment core ALB-1). The analysis was conducted on samples, presenting an average separation of 20 cm. The analysis reveals that the sediment is almost exclusively composed of quartz, calcite and clay minerals, the abundances of which vary widely along core. In order to obtain a more continuous record of these variations, we use a high-resolution Short-Wave InfraRed (SWIR) hyperspectral images (HSI) of sediment core ALB-1, a core retrieved from the delta of the Albegna River, in Tuscany, Italy, in 2020. The HSI is averaged over the characteristic thickness (3 cm) of each of the DRIFTS samples. A calibration of the HSI data using the DRIFTS data is then conducted. It allows converting the HSI into a continuous record of mineral abundances at a resolution of 3 cm. Tectosilicates in general, and quartz in particular, are not detected by SWIR-HIS. In the case at hand, however, the simplicity of the mineral assemblage allows to adduce quartz abundance from the abundance of the two other dominant mineral groups. We also attempt to provide a site-specific prediction of quartz by expecting inverse correlations with calcite or by grain-size texture effects. Practically, the method involves first the establishment of calibration curves of mineral assemblages and DRIFTS data using synthetic mixtures of minerals, in order to convert DRIFTS data into quartz, calcite, and clay content. The calibration is applied to convert the DRIFTS signature of 60 samples from core ALB-1 into mineral abundances. The sediment displays marked variations in grain-size (from clay to pebble) and of moisture content along core. The SWIR-HSI of untreated core surfaces is not only sensitive to carbonates and clay minerals content, but also to grain-size and

moisture. We consider as work hypothesis that calibration of HSI data with DRIFTS of dry and powdered samples could improve the continuous mineral logging along sediment cores. This treatment reveals sharp step-chances in mineral abundances along the core that were poorly visible in the discontinuous record, revealing the existence of very rapid (< 100 y), irreversible paleo-environmental changes. After exposing these results, we discuss several aspects of the methodology. We first discuss our selection of DRIFT spectra peaks to assess mineral abundances and the replicability of this approach. We then discuss the relevance of the approach presented here to the establishment of continuous records of mineral abundances in other geological settings. More generally, we discuss the complementarity, advantages and limits of using a two infrared sensors approach. Finally, we discuss the origin of the layering documented in core ALB-1 and the processes that control it.

2. General context

Core ALB-1 was retrieved in 2020 from the Holocene fluvio-deltaic plain of the Albegna River, in Tuscany, Italy (Fig.1). With a length of 70 km and a catchment area of 750 km², the Albegna River is one of the main coastal rivers of Tuscany. The river originates near the Quaternary Monte Amiata volcano, 1,738 m above sea-level (Fig. 1-A). The river flows south-westwards through Pliocene and Quaternary basins (Cornamusini et al., 2011; Bossio et al., 2004). It reaches the Thyrrenian Sea north of the Giannella sand spit (Fig.1-C). The tides along the Thyrrenian coast are microtidal averagely ranging ~ 30 cm (Bertoni et al., 2020). The climate in the area is Mediterranean, with a mean annual temperature of 13.8 °C along the coastal reaches and of 11°C in the Albegna headwaters. Mean annual precipitation ranges from 700 mm/year at the coast to 1500 mm/year on Monte Amiata (Marker et al., 2008). The Albegna River catchment drains Triassic-Cretaceous clayey calcareous limestones, succeeded downstream by Oligocene sandstone, Miocene lagoonal and marine deposits and finally Plio-Pleistocene marine clays close to the coast (Fig. 1-B, Cornamusini et al., 2011; Bossio et al., 2004; Bertini et al., 1967). A sizeable volume of sediments derived from these formations contributes to the > 30 m-thick Holocene infill of the Albegna lower valley, which was incised during the last glacial marine low stands (Mazzini et al., 1999). Geochemical and mineralogical data from widely scattered 30 surface silty-clay samples in the catchments of the Albegna and Fiora Rivers (Gliozzo et al., 2014) indicate mineral abundances in the range of 15-70% for phyllosilicates, 9- 58%

for quartz, and 1-34% for calcite. Phyllosilicates consist mainly of kaolinite, illite, smectite and chlorite. Feldspars (2-6%), dolomite (0-3%) and hematite (0-1%) are detected but are much less abundant.

3. Material and Methods

3.1. Field drilling

Mechanical rotation coring was conducted on the left bank of the Albegna River, +1.5 m above the mean sea-level, close to the river mouth (Fig. 1C), next to the historic Forte delle Saline Renaissance fortified tower, and next to the Roman fluvial port of Albinia. The site lies 200 m south of the Albegna River channel, 500 m east of the sea, and 700 m north of the lagoon of Orbetello. An outer core liner was used to prevent contamination of core sections by core wall material during drilling operations. Coring allowed the retrieval of a 14 m-long continuous sedimentary succession. Stratigraphic description in the field includes estimates of sediment color, texture, hardness, and the presence of oxidation, shells, and plant fragments. Absolute ages were obtained by accelerator mass spectrometry radiocarbon dating. The samples were process in the Center for Radiocarbon dating of Lyon UMR 5138, and measured at the LMC14 Artemis Laboratory in Saclay, France (Table 1). Radiocarbon ages were converted into calendar years using the IntCal20 Northern Hemishpere atmospheric calibration curve (Reimer et al., 2020).

3.2. Methodological approach

The approach involves five consecutive steps (Fig.2). The part of the sediment core comprised between 2 m and 13.5 m below the ground surface was extracted continuously using a 2 cm-wide plastic U-channel. A total of 11.5 meters, split into 23 U-channel sub-sections (50 cm each) were entirely scanned by SWIR-HSI (Step 1). U-channels prevent damaging of laminated sequences during transport, especially highly non-cohesive sand layers. After image acquisitions, sixty samples were taken from the U-channels (see section 3.2.2.) and measured by DRIFTS (Step 2). Synthetic mineral mixtures were prepared to calibrate the conversion of these DRIFTS data into mineral abundances (Step 3). DRIFTS and SWIR-HSI data were then compared over the areas of DRIFTS sampling to convert SWIR-HSI data into mineral abundances (Step 4). This calibration was then used to obtain a 3 cm-resolution continuous record of mineral abundances along the core (Step 5).

3.2.1. **Hyperspectral imaging** (Step 1)

Short-Wave Infrared (SWIR, Specim Ltd., Finland, OLES22.5) hyperspectral imaging of the sediment core was obtained following the protocol described in Jacq et al. (2020b). The resulting image is 1 cm wide and 11.5 m long. It consists of 45 columns and 53,220 lines of 185 μm^2-sized pixels. Each pixel contains a record of 288 individual spectral channels spanning a range of 3,880-10,354 cm^{-1}, corresponding to a wavelength range of 965 to 2,576 nm, with a 5.6 nm resolution. The spectra were subsampled between 3,966 and 9,781 cm^{-1} (1,016-2,526 nm) in order to remove noisy wavelengths. Reflectance spectra were then converted into pseudo-absorbance values, and pretreated by Standard Normal Variate and a baseline to be formatted in the same way as the DRIFTS data (Matlab R2020a, Mathworks, USA). SWIR-HSI spectra are presented in wavelength (nm) units.

3.2.2. **Sediment core sampling (Step 2)**

Magnetic susceptibility logging of the core (Dearing, 1999) was conducted at 3 cm-resolution using a Bartington MS2 susceptibilimeter and MS2F probe (Oxon, UK) in cgs units (centimeter-gram-second system) before the sampling of the core. Samples 3cm-thick were collected every 20 cm for DRIFTS (Figure 2, Step 2). Additional samples were collected in the thinnest stratigraphic units in order to prevent under-sampling of these units. The samples were dried in an oven at 50°C for seven days. The proportions of clay-silt, sand, and coarser fractions were measured by wet sieving through 0.063 mm and 2 mm-mesh size stainless steel sieves of 10 g of sediment. The sand fraction was sieved at 0.25, 0,5 and 1 mm to document grain-size distribution in the sand fraction (fine/medium/coarse sand). Subsamples of 5 g bulk sediment were set aside before the sieving and manually grinded using an agate mortar into a fine homogenous powder. The powder was dried at 50°C for 24h prior to spectroscopic measurement.

3.2.3. **Reference minerals and synthetic mineral assemblages (Step 3-A)**

42 synthetic mineral assemblages were produced for the calibration of the DRIFTS data. Powders of pure quartz (SiO2), calcite ($CaCO_3$), kaolinite ($Al_2Si_2O_5(OH)_4$), montmorillonite ($(Na,Ca)_{0,3}(Al,Mg)_2Si_4O_{10}(OH)_2$)) and illite ($K,H_3O(Al,Mg,Fe)_2(Si,Al)_4O_{10}[(OH)_2\cdot(H_2O)]$) were used from previously established mineral spectra databases (Chapkanski et al., 2021a,b). Samples (1 g each) of pure minerals were prepared by mixing oven-dried spectroscopic-grade potassium bromide (KBr) with

quartz (Q) and calcite (Ca). The clay minerals (Cm) were represented by a 1:1:1 mixture of kaolinite, montmorillonite and illite. Clay species can be successfully discriminated by FTIR spectroscopy (Srodo, 2002; Joussein et al., 2001), but, because their specific absorption bands overlap, it was decided to only consider their spectral signature collectively, to avoid any confusion (Muller et al., 2014). Further combinations were prepared: Q + Ca, Q + Cm, Ca + Cm and Q + Ca + Cm (Table 2). Precision of ± 0.1 mg is required when weighing. The powders were mixed by hand using an agate mortar and pestle for five minutes, in dry conditions. The samples were finally stored in an oven for 12 hours prior to spectroscopic measurement to maintain a low moisture content.

3.2.4. DRIFTS analysis (Step 3-B)

Diffuse Reflectance Infrared Fourier Transform Spectroscopy (DRIFTS) was conducted on the sediment core samples and on the synthetic mixtures. The texture of the powders ensures a good and homogenous penetration of infrared light into the samples (Bertaux et al., 1998). The mid-reflected infrared light spectrum of each sample was obtained using a FT-IR Frontier Spectrometer with a KBr beam splitter, a diffuse reflectance sampling accessory and a TGS detector (PerkinElmer, Waltham, MA, USA). Spectroscopic measurements were conducted in a temperature- and humidity-controlled room to ensure stable and constant optical air properties during measurement. 10 mg of each sample was placed into a micro-cup and scanned from 4,000 to 450 cm^{-1}, with a 1 cm^{-1} resolution, corresponding to wavelengths of 2,500 to 22,222 nm. Dried powdered potassium bromide (KBr) was used as background sample. Supplementary technical details are provided in Chapkanski et al., (2020). Middle Infrared spectral data feed a data matrix of “n” lines (where “n” is the number of spectra/samples) and “p” columns (where “p” is the quantity of spectral bands). The reflectance spectra were converted to absorbance, standardized, and finely baselined using Standard Normal Variate and Baseline pretreatments (Camo Unscrambler 10.3, Oslo, Norway). DRIFT spectra are presented in wavenumber (cm^{-1}) units.

3.3. Conversion of DRIFT spectra into mineral abundances (Step 3-C)

Absorbance mid-infrared spectroscopy has been applied to the quantification of mineral assemblages (Srodon, 2002) because the amount of absorbed infrared radiation is proportional to the mineral mass fraction (%weight), thus obeying to the Lamber-Beer’s law (Pichard and Frohlich, 1986; Bertaux et al.,

1998). Therefore, simple linear regressions (Moosavi and Ghassabian, 2018) can be applied to convert the areas of absorbance peaks into weight concentrations (Table 2). Spectroscopic measurements were repeated three times on each synthetic mixture to assess reproducibility. The most discriminating absorbance peaks were selected to quantify the %weight of each mineral species. The center of these peaks are located as follows: for quartz (Q) at 1,874 cm^{-1}, 1,160 cm^{-1}, and 696 cm^{-1}; for calcite (Ca) at 2,512 cm^{-1}, 875 cm^{-1}, and 848 cm^{-1}; and for clay minerals (Cm) at 3,696 cm^{-1}, 3,622 cm^{-1}, and 1,112 cm^{-1}. The baselined area of these peaks was quantified using the software PerkinElmer Spectrum (Waltham, MA, USA). Overlapping peak areas between the discriminating peaks were excluded to avoid over-quantification. Pure mineral end-members were used as zero-abundance standards for other end-member minerals. For instance, the pure quartz spectrum was used as standard zero for calcite calibration. Therefore, the linear regression was used to provide Q, Ca and Cm mineral weight estimates for each sample following: Mineral weight % = (peak area - a)/b. Linear coefficient of determination (R^2), mean values, and the standard deviations of residual values were used to evaluate the performance of the calibration (Moosavi and Ghassabian, 2018). Best curve calibrations were obtained at 1,160 cm^{-1} for quartz, 2,512 cm^{-1} for calcite, and 3,622 cm^{-1} for clays. The calibration was then used to quantify mineral species in the synthetic assemblages in order to evaluate the performance of the calibration on samples of known composition (Table 2). Finally, the calibration was used for the quantification of Q, Ca, and Cm abundances in the 60 samples of core ALB-1.

3.4. Calibration of HSI data for mineral abundance prediction (Step 4 and 5)

The hyperspectral image was down-sampled to a 3 cm-core thickness resolution over the areas occupied by each DRIFTS sample, such as to match the DRIFTS measurements. The DRIFTS-derived mineral abundance of the 60 sampling depth intervals (Fig. 2) was then matched to the corresponding SWIR-HSI spectra matrices. The two datasets were then subjected to partial least squares regressions (Wold et al., 1984) using the software Camo Unscrambler 10.3 (Oslo, Norway) to relate quartz, calcite and clay mineral abundances to the corresponding SWIR-HSI spectra obtained by hyperspectral imaging. Linear coefficients of determination (R^2) and root mean square errors (RMSE) were used to evaluate the performance of these regressions and p-values were provided to verify their statistical significances. Regression coefficient weight vectors of cumulated PLSR

components were used to assess the contribution of each wavelength to the correlation. The calibration was then used to assess the abundance of quartz, calcite, and clay minerals continuously along core ALB-1 at 3 cm-resolution using the SWIR-HSI spectral dataset, yielding a total of 313 measurements over the 14 m-long core. The same PLSR model was also applied to produce maps of mineral abundances. The same PLSR model was also applied to all the HSI pixels (45 columns by 53,220 lines) to produce mineral abundance maps and characterize the deposits at resolution of 185 µm.

4. Results

4.1. Stratigraphy, grain-size and magnetic susceptibility in core ALB-1

Sediment core ALB-1 intersected three main stratigraphic units (Fig.3). Basal Unit 1 (- 13.5 to - 8.5 m depth) is relatively homogenous and is composed of up to 70‰$_{wt}$ fine- to medium-sized grey shelly sand. Its magnetic susceptibility (MS) is low (0-80 cgs). Shell concentration is highest at its base (sub-unit 1-A) while the overlying sub-unit 1-B shows coarser and homogenous sands. Unit 2 (- 8.5 to - 3.5 m depth) is extremely heterogeneous and composed of alternations of silty clays and sand layers. Brownish, poorly magnetic silty clays at the base of unit 2 (in SU2-A) amount to 70‰$_{wt}$ of the sediment. The overlaying sub-unit 2-B is a succession of grey clayey/shelly sand and gravel. Magnetic values range from 0 to 300 cgs with marked peaks in coarse sand and gravely layers. The topmost sub-unit (2-C) is made of interbedded brown, weathered silty clay and sand layers. A well-sorted brown medium sand (70‰$_{wt}$ of the sand fraction) layer marks the top of sub-unit 2C. Magnetic susceptibly decreases upward throughout unit 2. The last, and topmost stratigraphic unit (SU3) consists of massive, weathered grey silty clay (90‰$_{wt}$ of the sediment) dotted by carbonate concretions near its base (SU3-A). Its upper part (SU3-B) is made of dark brown alternations of silty clay and sand containing roman pottery sherds with MS values ranging from 0 to 200 cgs.

4.2. Peak identification of Infrared spectra

4.2.1. DRIFT spectra of synthetic assemblages

A selection of DRIFT spectra of pure mineral species and species combination is provided on Figure 4. Quartz exhibits distinctive absorbance peaks at 1,872 cm^{-1}, 1,610 cm^{-1}, 1,352 cm^{-1}, 1,160 cm^{-1}, 813 cm^{-1} and 696 cm^{-1}. Calcite is identified by peaks at 2,984 cm^{-1}, 2,874 cm^{-1}, 2,512 cm^{-1}, 1,797 cm^{-1},

1,623 cm^{-1}, 1,400 cm^{-1}, 875 cm^{-1}, 848 cm^{-1}, and 714 cm^{-1}. Clays (kaolinite, montmorillonite, and illite) absorb mostly at 3,696 cm^{-1}, 3,624 cm^{-1}, 1,240 cm^{-1}, 1,111 cm^{-1} and 792 cm^{-1}.

4.2.2. DRIFT spectra of core samples

Figure 5 provides descriptive statistics (mean, maximum, minimum, Q1 and Q3 quartiles) of all combined core sample DRIFT spectra in the SWIR and MIR light ranges. Absorbance peaks were attributed to specific inorganic and organic compounds using previously established mineralogical spectra database (Chapkanski et al., 2021a,b) as well as extensive spectra libraries (Chukanov and Chervonnyi, 2016). Clay minerals, especially Kaolinite - $Al_2Si_2O_5(OH)_4$ and Montmorillonite - $(Na,Ca)_{0,3}(Al,Mg)_2Si_4O_{10}(OH)_2$) are associated with absorbance peaks at 3,696 and 3,626 cm^{-1} and around 3,400 to 3,350 cm^{-1} in the O - H stretching vibration region. Carbonates, especially calcite $CaCO_3$ is associated with absorbance peaks at 2,986 cm^{-1}, 2,876 cm^{-1}, 2,640 to 2,460 cm^{-1}, 1,460 to 1,360 cm^{-1} and 874 cm^{-1}. Tectosilicates, especially quartz (SiO_2) clearly absorb at 1,160 and 696 cm^{-1} while peak of feldspars occurs at 1,290 to 1,270 and 795 cm^{-1} and could be specifically attributed to albite $NaAlSi_3O_8$ and orthoclase $KAlSi_3O_8$. Inosilicate and nesosilicate minerals could absorb at 970 and 650 cm^{-1}. Chlorite and mica groups generated the absorbance peak observed at 1,630 cm^{-1}. Aliphatic C-H bands absorb at 2,930 cm^{-1} and unsaturated bands of alkenes C=C absorb at 1,642 cm^{-1}.

4.2.3. Short-Wave Infrared spectra of sediment core images

The SWIR spectra show areas of absorbance related to organic and inorganic compounds (Fig. 5). The two main absorption peaks near 1,440 nm and 1,925 nm are produced by hydroxyl bonds mainly induced by moisture (Palmer and Williams, 1974), but they can also be produced by organic and inorganic compounds, especially clays. Clays show absorption peaks related to Al-OH bonds between 2,200-2,220 nm and to O-H bonds around 1,410 nm, 2,340 nm and 2,450 nm (Madejova et al., 2017). Carbonates, chlorite and micas also produce multiple absorption peaks around 2,282 and between 2,310-2340 nm, but these often overlap with other compounds, such as organic matter (Cloutis, 1989; Krupnik and Khan, 2019; Viscarra Rossel and Behrens, 2010). Organic (C-H) bonds produce numerous absorption peaks, especially around 1,056 nm, 1,146 nm, 1,400 nm, 2,300-2,350 nm and

2,400-2,450 nm (Cloutis, 1989). Tectosilicates, including quartz, have no specific absorption peaks in the investigated spectral range (Krupnik and Khan, 2019).

4.3. Calibrations of mineral abundances

4.3.1 Performance of the synthetic sample cross-calibration

Weight concentrations (wt%) of minerals (quartz, calcite and clay minerals) were obtained using linear regression equations (Fig 6). Predicted values were plotted against known weight concentrations in order to evaluate the performance of the mineral quantifications (Fig. 6). Quartz, calcite and clay minerals were successfully predicted in single and multi-phase samples with R^2 > of 0.9. All correlations are significant with p-values < 0.05. Mean and standard deviations of residual values show slight underestimation of the prediction in single and multi-phases (from -0.5 to -1.5). The standard deviation ranges from 2.2 to 7.

4.3.2 Performance of the synthetic sample to core sample DRIFTS calibration

The linear regressions established using our synthetic standards were applied to the mid- infrared spectrum of the sediment cores samples (total of 60) to calculate quartz, calcite and clay minerals abundances (Fig. 3.C). Predicted values (in wt%) range between 14 and 64% (±0.2) for quartz, 0 and 43% (±0.7) for calcite, and 0 and 41% (±0.9) for clays. Quartz wt% is positively correlated with medium (0.48) and fine (0.53) sand fractions and bears negative correlation with the silty-clay (-0.56) fraction (Table 3). In contrast, clay minerals wt% is highly correlated to the clay-silt fraction (0.91) and negatively correlated to the medium (-0.78) and fine (-0.52) sand fractions. Calcite wt% shows no specific correlation with any grain-size fraction.

4.4 Calculation of mineral abundance along core ALB-1

4.4.1 Performance of the DRIFTS-core SWIR image calibration

Partial least squares regression (PLSR) was used to create a predictive model of quartz, calcite and clay abundance at regularly spaced, 3 cm-thick intervals along core ALB-1. The PLSR calibration was carried out between DRIFTS-derived mineral abundances in the 60 core samples and their SWIR spectra obtained by hyperspectral imaging (see section 3.4). The PLSR statistical performance is shown on Fig. 7. Quartz wt%, calcite wt%, and clay minerals wt% are successfully predicted based on

the SWIR spectra using seven latent variables (PLS components). In addition to statistical parameters, the plot analysis of the raw regression coefficients allows for evaluating the influence of absorbance bands on the PLS regression loading weights (Vogel et al., 2008; Hahn et al., 2011; 2018). High coefficients (either positive or negative) contribute significantly to the prediction of the major mineralogical components (Fig. 7). Calcite regression coefficients show positive values for spectral regions specific to carbonates (2,237 nm, 2,500 nm) and organic matter (1,056 nm, 1,146 nm), and negative values for spectral regions induced by clays (1,422 nm, 2,208 nm and 2,415 nm, Cloutis, 1989; Krupnik and Khan, 2019; Madejova et al., 2018; Viscarra Rossel and Behrens, 2010). Positive regression coefficients of clay minerals are related to specific wavelengths of phyllosilicates (1,411 nm, 1,900 nm, 2,202 nm and between 2,380-2,450 nm), while the negative coefficients are related to hydroxyl bonds probably induced by interstitial moisture between the coarser grains (1,445 nm, 1,838 nm, 1,945 nm) and to chlorites (2,292 nm, Palmer and Williams, 1974; Cloutis, 1989; Krupnik and Khan, 2019; Viscarra Rossel and Behrens, 2010). Quartz regression coefficients show positive values for spectral regions specific to hydroxyl bonds (1,445 nm and 1,945 nm) and stand out for their anti-correlation with carbonates (-0.82) and clay minerals (-0.42), particularly pronounced for the hydroxyl and carbonates bonds (2,237 nm, 2,500 nm, Fig. 7).

4.4.2. Performance of the continuous logging and mineral mapping along core ALB-1

The calibrated PLSR model was applied to each hyperspectral image data averaged over 3 cm bins, along the sediment (total of 313 bins) in order to assign continuous logging mineral abundances of quartz, calcite and clay minerals (Fig. 3.D). Predicted values range within 19-58% (±4) for quartz, 4-48% (±3) for calcite and 0-37% (±3) for clay minerals. They display a high degree of agreement with DRIFTS-derived abundances. Predicted quartz wt% is positively correlated with fine-sand (0.62) and total sand (0.60) fractions, and shows negative correlations with clay minerals (-0.68) and the clay-silt fraction (-0.58, Table 3). Predicted calcite wt% shows no specific correlations with other mineralogical or physical properties of sediments. Predicted clay minerals wt% show strong correlation with the clay-silt fraction (0.86) and hydroxyl bonds peak at 1,450 nm (0.68) and are negatively correlated to the total and medium sand fractions. The basal stratigraphic unit (SU1) is notably rich in quartz and poor in clay compared to other units. For SU1, differences between SWIR-HSI predicted and DRIFTS inferred mineral abundances are averagely 0.33, -0.44 and -0.27 for quartz, calcite and clays

respectively. The high resolution maps of mineral abundances (Fig.3D) reveal a faint layering produced by fluctuations in quartz abundance, while calcite and clay content remains fairly stable. The medium stratigraphic units (SU2) is highly heterogeneous, but it stands out for its higher calcite content than units SU1 and SU3, and for its higher clay content relative to SU1. For SU2, differences between predicted and observed mineral abundances are averagely -1.07, 0.26 and -0.35 for quartz, calcite and clays. SU3 is notably clay-rich and calcite-poor compared to the other units. For this unit, differences between predicted and observed mineral abundances are averagely 5.07, 0.17 and 1.34 for quartz, calcite and clays respectively.

5. Discussion

5.1. Peak selection for DRIFTS assessment of mineral abundances and replicability

Numerous studies reported satisfactory mineral calibrations and predictions using Fourier Transform InfraRed (FTIR) measurements on samples with known mineral contents (Pichard and Frohlich, 1986; Bertaux et al., 1998; Moosavi and Ghassabian, 2018). Based on these previous approaches, we converted DRIFTS data into mineral abundances using linear regressions calibrated on single and multi-phase synthetic mineral assemblages. Qualitatively, quartz, calcite and clay minerals can be identified easily in the infrared spectra (Fig. 4) owing to their specific peaks. In quantitative investigations, however, non-overlapping peaks should be selected (Pichard and Frohlich, 1986). Previous quantitative studies used peaks centered at 693 cm^{-1} and 712 cm^{-1} to respectively assess quartz and calcite abundances (Pichard and Frohlich, 1986). At these wavenumbers, however, overlaps with clay mineral peaks tend to generate unwanted quantitative distortions, so that better predictions were obtained using 1,160 cm^{-1} for quartz and 2,512 cm^{-1} for calcite. Calcite is the most abundant carbonate mineral in our sedimentary sequence, but its peak could be produced in other natural environments by additional carbonates, in particular aragonite (triple bond at 2,546, 2,524 and 2,500 cm^{-1}), dolomite (2,526 cm^{-1}) and magnesite (2,538 cm^{-1}). Among clay minerals, slight chemical variations can induce overlapping bonds (Madejova and Komadel, 2001) and different peak shapes (Henry et al., 2017). To overcome this problem, we have combined kaolinite, montmorillonite, and illite absorbances (Muller et al., 2014). The best calibration was obtained using a peak centered at 3,622 cm^{-1}, where the three clay species absorb. The accuracy of the linear regressions (Fig. 6) is satisfactory, with high R^2 coefficients, low residual values, and therefore a direct relationship between

absorbance and mineral abundance. Still, discrepancies between known single-phase mineral concentrations and DRIFTS-inferred abundances tend to increase at very low (< of 2%) and high (> of 50%) mineral concentration (Henry et al., 2017). Departure from the linear regression at high concentration could result from the lower density of the synthetic powder at such values, whereas departures at low concentration could be influenced by detection limits (Vogel et al., 2016). In multi-phase mineral concentrations, DRIFTS-inferred abundances remain satisfactory (Fig. 6) showing that the chosen peaks are not influenced by the absorbance of other minerals.

PLS regressions have been widely used to calibrate mineral abundances in FTIR spectra (Fernandes et al., 2020; Hahn et al., 2018; Muller et al., 2014). Predictions often show great performances and efficiency because the calibrations are based on the entire set of wavenumbers and therefore all absorbance peaks are considered. However, as certain peaks are common for two or more mineral phases, leading to over or under estimations (Vogel et al., 2016). Besides, the PLS calibration is population-specific, and must be rerun on each new dataset requiring the availability of the entire calibration dataset. However, these later are often inaccessible. To overcome this issue, this study provides linear regressions that are easily reusable for natural sediment spectra.

5.2. Calibration of high-resolution imaging SWIR spectra and DRIFTS-inferred mineral abundances

In the mid-infrared range used in DRIFTS, absorbance is controlled by vibrations of molecular bonds and functional groups. Therefore, peaks are very meaningful in the detection of carbonates and silicates (Fig. 5). By contrast, in the shorter infrared range (SWIR), absorbance is controlled by broad bonds, overtones and combination of functional groups (Robertson et al., 2016). Consequently, HSI-derived spectra are not sensitive to certain mineral phases such as tectosilicates (quartz and feldspar), some oxides, phosphates and sulfides (Krupnik and Khan, 2019). Moreover, spectral analyses are commonly based on chemometrics which, to overcome the absence of well-defined peaks, handle the entire range of wavelengths. Here, we use a PLS regression to assess the relationship between the DRIFTS-inferred mineral abundances and core image spectra, because the PLS regression allows us to assess the accuracy of the calibration. The analysis of PLS regression coefficients is commonly used to evaluate the performance of prediction models (Vogel et al., 2008; Hahn et al., 2011). Models relying on direct relationships between the investigated minerals and the

spectra (such as the SWIR-HSI models for calcite and clay minerals) are considered reliable and replicable because absorbance is directly influenced by specific functional bands in the crystalline structure of the minerals (Hahn et al., 2011, 2018). In contrast, models based on indirect relationships (such as the SWIR-HSI model for quartz) rely on inter-correlations between different mineralogical or physical properties that occur in specific sedimentological configurations and may, therefore, not be replicable elsewhere. In the present study, the good SWIR-HSI predictions of calcite and clay minerals result from a direct relationship to their respective functional groups. In the case of the clays, the correlation (> 0.60) that exists between clay minerals and clay-silt texture and hydroxyl bonds (see section 4.4.1, Table 3) may not result from intrinsic spectral properties of the clays, but rather from grain-size and moisture effects affecting the SWIR spectra. Nonetheless, dried and ground samples yield DRIFTS-derived abundance trends and values that are similar to that of the SWIR data implying that the SWIR-HSI prediction of clay minerals is mainly based on their spectral functional bonds, not by grain-size or moisture in the core. Similarly calcite predictions show no correlations with the physical properties of the core. By contrast, the acceptable prediction of quartz abundance by SWIR-HSI cannot result from the direct measurement of functional groups, as they do not reflect in that spectral range (see section 4.2.3.). The SWIR-HSI predicted quartz show significant positive correlations (> 0.60) with fine and total sand fractions (Table 3) and negative correlations (< -0.6) with the clay minerals. Moreover, the raw PLSR coefficients of quartz are negatively correlated (-0.82) with the calcite coefficients (Fig. 7). Therefore, quartz prediction by SWIR-HSI is made successful here owing to its close association to a fine and medium sand characterized by a relatively low calcite and clay mineral content, as opposed to silty-clay (rich of clay minerals) or shelly (rich of calcite) sediment with more heterogeneous textures. This association between well sorted, fine-to medium sand, and abundant quartz is a common characteristics of sediments that however is far from systematic. Therefore, the use of the methodology should be conducted with care, with a substantial site-specific foreknowledge of the sediment composition and of its variations. Used inappropriately, the model will generate significant inaccuracies.

5.3. Two-sensors infrared approach: complementarity, advantages and limits.

The two-sensor approach relies on the near- and mid-infrared electromagnetic ranges (Fig. 5). DRIFTS provides a precise quantification of quartz, calcite and clay minerals content owing to its high

sensitivity to specific functional bands in the mid-infrared range: O-H, N-H, C-H stretching, H-O-H deformation, CO_3, Si-O stretching, Si-O-Al and Fe-O (Russell & Fraser, 1994; Chukanov & Chervonnyi, 2016). The use of dried, ground samples ensures homogeneity and replicability of measurements. The analysis does not alter the chemistry and mineralogy of the samples, which can therefore be reused in other analyses. Compared to X-Ray Diffraction, DRIFTS is less sensitive to mineral phases present in small amount. However, is not subject to analytical biases introduced by the differential settling or preferred orientations of minerals (Herbert et al., 1992). Besides, owing to its wide range of wavenumbers (from 4.000 to 450 cm^{-1}), DRIFTS provides good qualitative determination of clay minerals directly on bulk sediments and it is sensitive to both amorphous silica (Meyer-Jacob et al., 2014; Frohlich, 1989) and organic compounds (Francos et al., 2021; Chapman et al., 2001). Therefore, it constitutes a relevant alternative to conventional XRD for the calibration of mineral abundance based on hyperspectral images (Greene et al., 2019). To conduct an optimal HSI modelling, calibration samples should cover the entire range of mineral concentrations (Vogel et al., 2008), which is found in the image. To capture the expected range, samples should be collected at regular, and rather short depth-intervals along the core, generating a sizeable number of samples. To process such a large number of samples, DRIFTS is also appropriate because it can be carried out on small (10 mg) samples, because it do not involve hazardous chemical materials nor dangerous radiation emissions. Sample preparation is quick (~1 min/sample) and simple. The establishment of the calibration curves using synthetic mixtures is the most time-consuming step, but future users can simply reuse the linear regression coefficients provided in this study in order to obtain (semi) quantitative mineral abundances from the DRIFT spectra of natural sediments.

Although near-infrared spectra obtained by hyperspectral core-imaging are less sensitive to mineral composition and not sensitive to tectosilicates, they provide unprecedented time-saving (2 min/meter), high-resolution investigations (185 μm^2 pixel) in a completely non-invasive and non-destructive manner. The main challenges arise from the irregular and heterogeneous state of the sediment core surface, which often presents particle size and humidity variations that strongly impact the near infrared spectrum, leading to prediction bias (Verpoorter et al., 2014). For this reason, calibrations with mineral abundance values inferred by the DRIFTS on powdered and dry samples constraint the PLSR algorithm to specific-absorbance of minerals and reduce the effects of moisture and grain-size. The latter can be easily detected using two main absorptions bands by O-H bonds around 1,440 nm

and 1,925 nm, but also by the rise of the spectra baseline in the Near- and Mid-Infrared ranges (Fig 5). In the present study, low deviations between DRIFTS-inferred and SWIR-HSI predictions of minerals (< 1.5, see section 4.4.2.) suggest that the heterogeneous grain-size state of the sediment core surface is overcome by the PLSR modelling. By contrast, the prediction of quartz remains strongly dependent of site-specific sediment and mineralogical characteristics.

5.4. Depositional environments encountered along core ALB-1

The palaeovalley of the Albegna River has been incised during the last glacial sea-level low stands; it was subsequently infilled by marine and fluvial sediments during the Late-glacial to Holocene transgression (Mazzini et al., 1999). The delta of the Albegna River has progressively prograded and filled its valley, while a sand-spit was building up farther offshore, progressively isolating a lagoon from the open sea. The delta is therefore expected to have grown first in an open marine environment, and then in a lagoonal environment, before reaching the sand spit and shedding its sediment, along the sand spit foreshore. The core is located within the former lagoon, immediately behind the sand spit, at a location that probably emerged just as the emerged delta floodplain was reaching the sand spit,

Non-continuous grain-size analysis, continuous magnetic susceptibility, and mineral core-logging reveal three stratigraphic units, which we subdivided into two-three sub-units (Fig. 3). The lower sequence SU1 contains thin (1 cm-thick) silty-clay layers interbedded with fine- to medium- grained, quartz-rich sand containing occasional shells and well-rounded gravel. Considering its age (> 5,300 BCE), unit SU1 can be interpreted as deposited in an open marine environment, during the transgression and maximum flooding of the Albegna palaeo-valley. The slight upward coarsening, from SU1-A to SU1-B, may reflect the progradation of the Albegna River delta (Styllas, 2014) after the maximum flooding. It is associated with a slight but continuous increase in quartz abundance, which may result from the positive correlation between quartz abundance and sand grain size. The continuous record (Fig. 3D) reveals an abrupt superposition of the overlying deposits (SU2-1), composed of organic clays. This facies is reminiscent of the quiet lagoonal environment still found today in the remain parts of the lagoon, and is therefore interpreted as resulting from the rapid development of lagoonal conditions behind the sand spit (5,500 to 5,370 BCE) during the Atlantic.

This unit is overlaid by extremely heterogeneous sediments (SU2-B) consisting of fine- to medium-grained sand deposits interbedded with silty-clayey layers. Calcite content is at its highest and correlates with layers of medium- to coarse-grained sand made of shell fragments. This facies indicates a highly biologically productive in the shallow lagoon occurring between 4,240 and 4,000 BCE) at the end of the Atlantic. The greater abundance of sand, compared to the lagoon of Orbetello farther south, indicates the proximity of either an inlet in the sand spit, or/and, most likely, the increasing proximity of the Albegna River mouth, as the river delta progrades across the lagoon toward the coring site. Local peaks in magnetic susceptibility are produced by gravely beds rich in shell fragments and may represent the reworking of the coarsest river sediments. The SU2-B to SU2-C evolution from a reducing to oxidizing environment (grey to brown-colored sediments) and the increase in grain-size (from fine-medium- to coarse-grained sand) reflects the progressive shoaling of the lagoon, as the Albegna River mouth gets closer to the coring site. The highest unit (SU3) is composed of emerged floodplain sediments, deposited on the banks of the Albegna River, once the coring site had been integrated into its delta plain between 2,880 and 2,630 cal BC, during the Subboreal. The overbank deposits consist of weathered silty-clay, rich in clay minerals, cemented by carbonate concretions deposited near the water table. The top of the core (SU3-B) consists of dark-brown silty-clay and unsorted sands. Its dark brownish color may reflect more advanced pedogenesis, in a floodplain progressively less frequently subjected to flooding. However, interpretation is made difficult by the fact that this sediment has been strongly reworked by anthropogenic activity, which is attested by the high density of Roman sherds in this top unit.

5.5. Wider significance

The widespread use of sediment cores for a variety of environmental research, mining and civil engineering applications provides a favorable context for the development of fast techniques that do not require time-consuming pretreatments with chemical products. The need for fast and easily applied techniques encourages approaches based on continuous core-logging calibrated on punctual analyses (Greene et al., 2019). The two-sensor infrared methodology proposed here, involving DRIFTS and SWIR-HSI for the continuous logging of mineral abundances along sediment cores, provides a simple and time-saving approach. Hyperspectral imaging has already demonstrated its added value in the study of lacustrine environments (Sorrel et al., 2021; Makri et al., 2020; Butz et al.,

2017; Aymerich et al., 2016). Its application to a wider range of sedimentary environments remains to be tested, especially in contexts, such as here, where substantial grain-size variations occur along core. Here our combined two infrared sensor approach shows sharp mineralogical variations between subunits and within subunits. The maps of mineral abundances provide extremely high-resolution horizontal and vertical values of abundances, highlighting laminations and the fine-scale architecture of the sediment layers. Our analysis, albeit restricted to three major mineral species and groups, illustrates variations that can be tied to major changes in the depositional environment (open sea, lagoonal, fluvio-deltaic). We believe that the high resolution prediction of calcite and clay minerals could be easily applied in other sedimentological environments, but for prediction of quartz we rather recommend to use Mid-Wave InfraRed (MWIR: 2,700-5,300 nm) or Long-Wave InfraRed (LWIR: 8,000-12,000 nm) hyperspectral cameras (Contreras Acosta et al., 2020; Lorenz et al., 2019) that are sensible to tectosilicates. To improve processing times, benchtop DRIFTS measurements could be replaced by the emerging hand-operated FTIR, but the use of such non-destructive techniques has to reckon with issues of sample humidity and grainsize variations at the sediment surface. Wider significance of this approach would be found in geoarchaeological stratigraphy (Haburaj et al., 2020; Linderholm et al., 2018) and sequence stratigraphy where hyperspectral imaging could be correlated with Ground Penetrating Radar (GPR) profiles. Moreover, in palaeo-lagoon investigations correlated with seasonal variations of macro- and micro-fauna.

6. Conclusion

This study demonstrates the potential of a two-sensor infrared methodology involving Diffuse Reflectance Infrared Fourier Transform spectroscopy (DRIFTS) and Short-Wave InfraRed (SWIR) hyperspectral imaging (HSI) to provide a simple and time-saving approach for continuous logging of mineral abundances along sediment cores. The DRIFT spectra were used to provide quantitative estimations for quartz, calcite and clay minerals abundances of single and multi-phase synthetic mixtures. Therefore, reliable DRIFTS-inferred estimations of these minerals were obtained for 60 sediment samples from a 14 meters-depth core (ALB-1), drilled in the deltaic deposits of the Albegna River. The mineral abundance values were fused with the SWIR-HSI data in order to establish partial least squares regression (PLSR) model aiming to assign continuous logging of mineral abundances

along the ALB-1 core. The PLSR statistical performance was satisfactory showing high degree of agreement between the DRIFT-induced and SWIR-HSI predicted results. The same predicting model was used to compute maps of mineral abundances evidencing the layered structure of mineral concentrations. The classical sedimentological non-continuous analyses (e.g. grain-size), complemented by combined DRIFTS and SWIR-HSI approach, bring into focus changes of sediment dynamics and depositional patterns recorded into the deltaic facies at high-resolution vertical scale. We contend here that the fused two-sensor infrared approach has a clear potential to help reconstructing fluvial-deltaic sedimentary successions. Calcite and clay minerals could be reliably predicted in other sedimentary environments. However, in terms of quartz prediction, the SWIR-HSI remain limited and it cannot be used for direct spectra modeling of tectosilicates. To overcome this issue, we rather recommend to use Mid-Wave InfraRed (MWIR: 2,700-5,300 nm) or Long-Wave InfraRed (LWIR: 8,000-12,000 nm) hyperspectral cameras. However, these latter significantly costlier. Further analyses are intended in order to provide quantifications of specific phyllosilicates (kaolinite vs. illite vs. smectite) by DRIFTS in order to test whether they could be reliably predicted by SWIR-HSI in complex fluvio-deltaic sediment mixtures. Moreover, research involving DRIFT-induced total organic matter and biogenic silica abundances are currently in progress in order to provide a wider understanding of the total sample composition.

7. Acknowledgement

This research was conducted in the framework of the IDEX-Lyon Scientific Breakthrough Program: "*Thalassocraties sans ports: fait ou fiction?"* directed by Jean-Philippe Goiran and funded by the National Agency for Research. Further financial assistance came from the Mobility program SMI-INSHS-CNRS and LabEx IMU programe: URBO, led by Jean-Philippe Goiran. The Alexander von Humboldt Foundation, Germany, generously accorded additional funding to the project and Andrea U. De Giorgi. The study is conducted in close cooperation with the *Soprintendenza Archeologica Belle Arti e Paesaggio per le Province di Siena, Grosseto e Arezzo,* the World Wide Fund for Nature (WWF Oasi), the Municipality of Orbetello and the French National Centre for Scientific Research CNRS. The equipment and facilities permitting DRIFTS measurements were co-founded by the LabCom Geo-Heritage (ANR-15-LCV4-0002), University of Lyon 2, IDEX-Lyon Scientific Breakthrough Program, European Research Council (Grant Agreement 339123) and the University of Paris 1

Pantheon-Sorbonne. The hyperspectral imaging acquisition was made at the University of Normandie-Rouen and was funded by the Region Normandie, which supports the scientific consortium SCALE UMR CNRS 3730. The authors are grateful to Dr. Matteo Milletti and Salvatore Russo for their help at the field in the *Torre Saline* Area as well, Mauro and Barbara for their help with the accommodation, Maureen le Doaré for the stratigraphic computer assistant drawing and Maël Ogier for the help with the wet sieving and magnetic susceptibility measurements. The authors thank gratefully the two anonymous reviewers for their constructive and detailed feedbacks permitting to improve earlier versions of this manuscript.

8. Data Availability

All the data that support the findings of this study are available from the corresponding author upon reasonable request.

References

Andrews, J. T., & Eberl, D. D. 2012. Determination of sediment provenance by unmixing the mineralogy of source-area sediments: the “SedUnMix” program. Marine Geology, 291, 24-33.

Aymerich, I. F., Oliva, M., Giralt, S., & Martín-Herrero, J. 2016. Detection of tephra layers in Antarctic sediment cores with hyperspectral imaging. PLoS One, 11(1), e0146578.

Bandopadhyay, A. K. 2010. Determination of quartz content for Indian coals using an FTIR technique. International Journal of Coal Geology, 81(1), 73-78.

Bertaux, J., Froehlich, F., & Ildefonse, P. 1998. Multicomponent analysis of FTIR spectra; quantification of amorphous and crystallized mineral phases in synthetic and natural sediments. Journal of Sedimentary Research, 68(3), 440-447.

Bertoni, D., Giacomelli, S., Ciulli, L., & Sarti, G. 2020. Litho-sedimentological and morphodynamic characterization of the Pisa Province coastal area (northern Tuscany, Italy). *Journal of Maps*, *16*(2), 108-116.

Bertini, M., Cocozza, T., Signorini, R. 1967. Carta geologica d’Italia, Orbetello, Foglio 135, Ser. Geol. Italia.

Bigus, P., Tobiszewski, M., & Namieśnik, J. 2014. Historical records of organic pollutants in sediment cores. Marine pollution bulletin, 78(1-2), 26-42.

Bosch-Reig, F., Gimeno-Adelantado, J. V., Bosch-Mossi, F., & Doménech-Carbó, A. 2017. Quantification of minerals from ATR-FTIR spectra with spectral interferences using the MRC method. Spectrochimica Acta Part A: Molecular and Biomolecular Spectroscopy, 181, 7-12.

Bossio, A., Foresi, L. M., Mazzei, R., Salvatorini, G., Sandrelli, F., Bilotti, M., ... & Rossetto, R. 2003. Geology and stratigraphy of the southern sector of the Neogene Albegna River Basin (Grosseto, Tuscany, Italy). Geologica Romana, 37(2003-2004), 165-173.

Butz, C., Grosjean, M., Goslar, T., & Tylmann, W. 2017. Hyperspectral imaging of sedimentary bacterial pigments: a 1700-year history of meromixis from varved Lake Jaczno, northeast Poland. Journal of Paleolimnology, 58(1).

Chapkanski, S., Ertlen, D., Rambeau, C., & Schmitt, L. 2020. Provenance discrimination of fine sediments by mid-infrared spectroscopy: Calibration and application to fluvial palaeo-environmental reconstruction. Sedimentology, 67(2), 1114-1134.

Chapman, S. J., Campbell, C. D., Fraser, A. R., & Puri, G. 2001. FTIR spectroscopy of peat in and bordering Scots pine woodland: relationship with chemical and biological properties. Soil Biology and Biochemistry, 33(9), 1193-1200.

Chukanov, N. V., & Chervonnyi, A. D. 2016. Infrared spectroscopy of minerals and related compounds. Springer.

Cloutis, E. A. 1989. Spectral reflectance properties of hydrocarbons: Remote-sensing implications. Science, 245(4914), 165–168.

Contreras Acosta, I. C., Khodadadzadeh, M., Tolosana Delgado, R., & Gloaguen, R. 2020. Drill-core hyperspectral and geochemical data integration in a superpixel-based machine learning framework. IEEE Journal of Selected Topics in Applied Earth Observations and Remote Sensing, 1–16. https://doi.org/10.1109/JSTARS.2020.3011221

Cornamusini, G., Foresi, L. M., Massa, G., Bonciani, F., Callegari, I., Da Prato, S., & Ielpi, A. 2011. The Miocene successions of the Fiora Hills: considerations about the development of the minor basins of Southern Tuscany. Italian Journal of Geosciences, 130(3), 404-424.

Davies, S. J., Lamb, H. F., & Roberts, S. J. 2015. Micro-XRF core scanning in palaeolimnology: recent developments. Micro-XRF studies of sediment cores, 189-226.

Dearing, J. 1999. Environmental magnetic susceptibility using the Bartington MS2 system. Bartington Instruments Ltd. British Library London.

Delile, H., Goiran, J. P., & Blichert-Toft, J. 2018. The contribution of geochemistry to ancient harbor geoarcheology: The example of Ostia Antica. Quaternary Science Reviews, 193, 170-187.

Duée, C., Orberger, B., Maubec, N., Laperche, V., Capar, L., Bourguignon, A., ... & Koert, P. 2019. Impact of heterogeneities and surface roughness on pXRF, pIR, XRD and Raman analyses: challenges for on-line, real-time combined mineralogical and chemical analyses on drill cores and implication for “high speed” Ni-laterite exploration. Journal of Geochemical Exploration, 198, 1-17.

Fernandes, K., Júnior, J. M., de Souza Bahia, A. S. R., Demattê, J. A., & Ribon, A. A. 2020. Landscape-scale spatial variability of kaolinite-gibbsite ratio in tropical soils detected by diffuse reflectance spectroscopy. Catena, 195, 104795.

Francos, N., Ogen, Y., & Ben-Dor, E. 2021. Spectral assessment of organic matter with different composition using reflectance spectroscopy. Remote Sensing, 13(8), 1549.

Frei, R. W., & MacNeil, J. D. 2019. Diffuse reflectance spectroscopy in environmental problem-solving. CRC press.

Fröhlich, F. (1989). Deep-sea biogenic silica: new structural and analytical data from infrared analysis-geological implications. Terra nova, 1(3), 267-273.

Garzanti, E., Andó, S., France-Lanord, C., Censi, P., Vignola, P., Galy, V., & Lupker, M. 2011. Mineralogical and chemical variability of fluvial sediments 2. Suspended-load silt (Ganga–Brahmaputra, Bangladesh). Earth and Planetary Science Letters, 302(1-2), 107-120.

Garzanti, E., Andò, S., France-Lanord, C., Vezzoli, G., Censi, P., Galy, V., & Najman, Y. 2010. Mineralogical and chemical variability of fluvial sediments: 1. Bedload sand (Ganga–Brahmaputra, Bangladesh). Earth and Planetary Science Letters, 299(3-4), 368-381.

Ghanbari, H., Jacques, O., Adaïmé, M. É., Gregory-Eaves, I., & Antoniades, D. 2020. Remote Sensing of Lake Sediment Core Particle Size Using Hyperspectral Image Analysis. Remote Sensing, 12(23), 3850.

Gliozzo, E., Iacoviello, F., & Foresi, L. M. 2014. Geosources for ceramic production: The clays from the Neogene–Quaternary Albegna Basin (southern Tuscany). Applied clay science, 91, 105-116.

Greene, J., Kosanke, T. H., & Linton, P. EA. 2019. Quantitative Calibration of Hyperspectral Core Imaging Data: A New Method for Producing Continuous, High-Resolution Mineralogical Characterization of Cores from Both Conventional and Unconventional Reservoirs. Annual Convention and Exhibition (AAPG). 0-20.

Haburaj, V., Japp, S., Gerlach, I., Hoelzmann, P., & Schütt, B. 2020. Coupling spectral imaging and laboratory analyses to digitally map sediment parameters and stratigraphic layers in Yeha, Ethiopia. Plos one, 15(9), e0238894.

Hahn, A., Gerdts, G., Völker, C., & Niebühr, V. 2019. Using FTIRS as pre-screening method for detection of microplastic in bulk sediment samples. Science of the total environment, 689, 341-346.

Hahn, A., Rosen, P., Kliem, P., Ohlendorf, C., & Zolitschka, B. 2011. Comparative study of infrared techniques for fast biogeochemical sediment analyses. Geochemistry, Geophysics, Geosystems, 12(10).

Hahn, A., Vogel, H., Andó, S., Garzanti, E., Kuhn, G., Lantzsch, H., Schuurman J., Vogt C., & Zabel, M. 2018. Using Fourier transform infrared spectroscopy to determine mineral phases in sediments. Sedimentary geology, 375, 27-35.

Hamdan, M. A., Hassan, F. A., Flower, R. J., Leroy, S. A. G., Shallaly, N. A., & Flynn, A. 2019. Source of Nile sediments in the floodplain at Saqqara inferred from mineralogical, geochemical, and pollen data, and their palaeoclimatic and geoarchaeological significance. Quaternary international, 501, 272-288.

He, J., Garzanti, E., Dinis, P., Yang, S., & Wang, H. 2020. Provenance versus weathering control on sediment composition in tropical monsoonal climate (South China)-1. Geochemistry and clay mineralogy. Chemical Geology, 558, 119860.

Henry, D. G., Watson, J. S., & John, C. M. 2017. Assessing and calibrating the ATR-FTIR approach as a carbonate rock characterization tool. Sedimentary geology, 347, 36-52.

Herbert, T. D., Tom, B. A., & Burnett, C. 1992. Precise major component determinations in deep-sea sediments using Fourier Transform Infrared Spectroscopy. Geochimica et Cosmochimica Acta, 56(4), 1759-1763.

Heroy, D. C., Kuehl, S. A., & Goodbred Jr, S. L. 2003. Mineralogy of the Ganges and Brahmaputra Rivers: implications for river switching and Late Quaternary climate change. Sedimentary Geology, 155(3-4), 343-359.

Jacq, K., Giguet-Covex, C., Sabatier, P., Perrette, Y., Fanget, B., Coquin, D., Debret, M., & Arnaud, F. (2019). High-resolution grain size distribution of sediment core with hyperspectral imaging. Sedimentary Geology, 393, 105536.

Jacq, K., Martinez-Lamas, R., Van Exem, A., & Debret, M. 2020. Hyperspectral core-logger image acquisition. In Protocols.io. https://protocols.i/view/hyperspectral-core-logger-image-acquisition-bikckcsw

Jacq, K., Perrette, Y., Fanget, B., Sabatier, P., Coquin, D., Martinez-Lamas, R., Debret, M., & Arnaud, F. 2019. High-resolution prediction of organic matter concentration with hyperspectral imaging on a sediment core. Science of the Total Environment, 663, 236-244.

Joussein, E., Petit, S., & Decarreau, A. 2001. Une nouvelle méthode de dosage des minéraux argileux en mélange par spectroscopie IR. Comptes Rendus de l'Académie des Sciences-Series IIA-Earth and Planetary Science, 332(2), 83-89.

Kahraman, S., Rostami, J., & Naeimipour, A. 2016. Review of ground characterization by using instrumented drills for underground mining and construction. Rock Mechanics and Rock Engineering, 49(2), 585-602.

Kelsey, H. M., Engelhart, S. E., Pilarczyk, J. E., Horton, B. P., Rubin, C. M., Daryono, M. R., Ismail, N., Hawkes, A. D., Bernhardt, C. E., & Cahill, N. 2015. Accommodation space, relative sea level, and the archiving of paleo-earthquakes along subduction zones. Geology, 43(8), 675-678.

Krupnik, D., & Khan, S. (2019). Close-range, ground-based hyperspectral imaging for mining applications at various scales: Review and case studies. Earth-Science Reviews, 198, 34. https://doi.org/10.1016/j.earscirev.2019.102952

Larkin, P. 2017. Infrared and Raman spectroscopy: principles and spectral interpretation. Elsevier.

Li, J., Hu, B., Wei, H., Zhao, J., Zou, L., Bai, F., Dou, Y., Wang, L., & Fang, X. 2014. Provenance variations in the Holocene deposits from the southern Yellow Sea: clay mineralogy evidence. Continental Shelf Research, 90, 41-51.

Linderholm, J., Geladi, P., Gorretta, N., Bendoula, R., & Gobrecht, A. 2019. Near infrared and hyperspectral studies of archaeological stratigraphy and statistical considerations. Geoarchaeology, 34(3), 311-321.

Liu, J., Zhang, J., Miao, X., Xu, S., & Wang, H. 2020. Mineralogy of the core YRD-1101 of the Yellow River Delta: Implications for sediment origin and environmental evolution during the last~ 1.9 Myr. Quaternary International, 537, 79-87.

Lorenz, S., Seidel, P., Ghamisi, P., Zimmermann, R., Tusa, L., Khodadadzadeh, M., Contreras, I. C., & Gloaguen, R. 2019. Multi-Sensor Spectral Imaging of Geological Samples: A Data Fusion

Approach Using Spatio-Spectral Feature Extraction. Sensors, 19(12), 2787. https://doi.org/10.3390/s19122787

Lupker, M., France-Lanord, C., Galy, V., Lavé, J., Gaillardet, J., Gajurel, A. P., Guilmette, C., Rahman, M., Singh, S. K., & Sinha, R. 2012. Predominant floodplain over mountain weathering of Himalayan sediments (Ganga basin). Geochimica et Cosmochimica Acta, 84, 410-432.

Madejova, J., & Komadel, P. 2001. Baseline studies of the clay minerals society source clays: infrared methods. Clays and clay minerals, 49(5), 410-432.

Madejová, J., Gates, W.P., Petit, S. 2017. IR Spectra of Clay Minerals. In: Developments in Clay Science 107–149.

Makri, S., Rey, F., Gobet, E., Gilli, A., Tinner, W., & Grosjean, M. 2020. Early human impact in a 15,000-year high-resolution hyperspectral imaging record of paleoproduction and anoxia from a varved lake in Switzerland. Quaternary science reviews, 239, 106335.

Makri, S., Rey, F., Gobet, E., Gilli, A., Tinner, W., & Grosjean, M. 2020. Early human impact in a 15,000-year high-resolution hyperspectral imaging record of paleoproduction and anoxia from a varved lake in Switzerland. Quaternary science reviews, 239, 106335.

Märker, M., Angeli, L., Bottai, L., Costantini, R., Ferrari, R., Innocenti, L., & Siciliano, G. 2008. Assessment of land degradation susceptibility by scenario analysis: A case study in Southern Tuscany, Italy. Geomorphology, 93(1-2), 120-129.

Martinelli, L. A., Victoria, R. L., Dematte, J. L. I., Richey, J. E., & Devol, A. H. 1993. Chemical and mineralogical composition of Amazon River floodplain sediments, Brazil. Applied Geochemistry, 8(4), 391-402.

Mazzini, I., Anadon, P., Barbieri, M., Castorina, F., Ferreli, L., Gliozzi, E., Mola, M., & Vittori, E. (1999). Late Quaternary sea-level changes along the Tyrrhenian coast near Orbetello (Tuscany, central Italy): palaeoenvironmental reconstruction using ostracods. Marine Micropaleontology, 37(3-4), 289-311.

Melucci, D., Zappi, A., Poggioli, F., Morozzi, P., Giglio, F., & Tositti, L. 2019. ATR-FTIR spectroscopy, a new non-destructive approach for the quantitative determination of biogenic silica in marine sediments. Molecules, 24(21), 3927.

Meyer-Jacob, C., Vogel, H., Boxberg, F., Rosén, P., Weber, M. E., & Bindler, R. 2014. Independent measurement of biogenic silica in sediments by FTIR spectroscopy and PLS regression. Journal of paleolimnology, 52(3), 245-255.

Miller, C., Hahn, A., Liebrand, D., Zabel, M., & Schefuß, E. 2020. Mid-and low latitude effects on eastern South African rainfall over the Holocene. Quaternary Science Reviews, 229, 106088.

Milosevic, M. (2012). Internal reflection and ATR spectroscopy (Vol. 176). John Wiley & Sons.

Moore, D. M., & Reynolds Jr, R. C. 1989. X-ray Diffraction and the Identification and Analysis of Clay Minerals. Oxford University Press (OUP).

Moosavi, S. M., & Ghassabian, S. 2018. Linearity of calibration curves for analytical methods: A review of criteria for assessment of method reliability. Calibration and Validation of Analytical Methods: A Sampling of Current Approaches; IntechOpen Limited: London, UK, 109-127.

Moros, J., Vallejuelo, S. F. O. D., Gredilla, A., Diego, A. D., Madariaga, J. M., Garrigues, S., & Guardia, M. D. L. 2009. Use of reflectance infrared spectroscopy for monitoring the metal content of the estuarine sediments of the Nerbioi-Ibaizabal River (Metropolitan Bilbao, Bay of Biscay, Basque Country). Environmental science & technology, 43(24), 9314-9320.

Müller, C. M., Pejcic, B., Esteban, L., Delle Piane, C., Raven, M., & Mizaikoff, B. 2014. Infrared attenuated total reflectance spectroscopy: an innovative strategy for analyzing mineral components in energy relevant systems. Scientific reports, 4(1), 1-11.

Painter, P. C., Coleman, M. M., Jenkins, R. G., Whang, P. W., & Walker Jr, P. L. 1978. Fourier Transform Infrared study of mineral matter in coal. A novel method for quantitative mineralogical analysis. Fuel, 57(6), 337-344.

Palmer, K. F., & Williams, D. 1974. Optical Properties of Water in the Near Infrared. Journal of Optical Society of America, 64(8), 1107–1110. https://doi.org/10.1364/JOSA.64.001107

Paris, R., Falvard, S., Chagué, C., Goff, J., Etienne, S., & Doumalin, P. 2020. Sedimentary fabric characterized by X-ray tomography: a case-study from tsunami deposits on the Marquesas Islands, French Polynesia. Sedimentology, 67(3), 1207-1229.

Pennington, B. T., Sturt, F., Wilson, P., Rowland, J., & Brown, A. G. 2017. The fluvial evolution of the Holocene Nile Delta. Quaternary Science Reviews, 170, 212-231.

Pe-Piper, G., Piper, D. J., Wang, Y., Zhang, Y., Trottier, C., Ge, C., & Yin, Y. 2016. Quaternary evolution of the rivers of northeast Hainan Island, China: tracking the history of avulsion from mineralogy and geochemistry of river and delta sands. Sedimentary Geology, 333, 84-99.

Pichard, C., & Frohlich, F. 1986. Analyses IR quantitatives des sédiments. Exemple du dosage du quartz et de la calcite. Revue de l'Institut français du pétrole, 41(6), 809-819.

Pre, C. A. G., Horton, B. P., Kelsey, H. M., Rubin, C. M., Hawkes, A. D., Daryono, M. R., Rosenberg, G., & Culver, S. J. 2012. Stratigraphic evidence for an early Holocene earthquake in Aceh, Indonesia. Quaternary Science Reviews, 54, 142-151.

Rapuc, W., Jacq, K., Develle, A. L., Sabatier, P., Fanget, B., Perrette, Y., Coquin, D., Debret, M., Wilhelm, B., & Arnaud, F. 2020. XRF and hyperspectral analyses as an automatic way to detect flood events in sediment cores. Sedimentary Geology, 409, 105776.

Reimer, P., Austin, W., Bard, E., Bayliss, A., Blackwell, P., Bronk Ramsey, C., Butzin, M., Cheng, H., Edwards, R., Friedrich, M., Grootes, P., Guilderson, T., Hajdas, I., Heaton, T., Hogg, A., Hughen, K., Kromer, B., Manning, S., Muscheler, R., Palmer, J., Pearson, C., van der Plicht, J., Reimer, R., Richards, D., Scott, E., Southon, J., Turney, C., Wacker, L., Adolphi, F., Büntgen, U., Capano, M., Fahrni, S., Fogtmann-Schulz, A., Friedrich, R., Köhler, P., Kudsk, S., Miyake, F., Olsen, J., Reinig, F., Sakamoto, M., Sookdeo, A., & Talamo, S. (2020). The IntCal20 Northern Hemisphere radiocarbon age calibration curve (0–55 cal kBP). Radiocarbon, 62.

Rivard, B., Harris, N. B., Feng, J., & Dong, T. 2018. Inferring total organic carbon and major element geochemical and mineralogical characteristics of shale core from hyperspectral imaging. AAPG Bulletin, 102(10), 2101-2121.

Robertson, A. J., Shand, C., & Perez-Fernandez, E. 2016. The application of Fourier transform infrared, near infrared and X-ray fluorescence spectroscopy to soil analysis. Spectroscopy Europe, 28(4), 9-13.

Rosén, P., Vogel, H., Cunningham, L., Hahn, A., Hausmann, S., Pienitz, R., Zolitschka, B., Wagner, B., & Persson, P. 2011. Universally applicable model for the quantitative determination of lake sediment composition using Fourier transform infrared spectroscopy. Environmental science & technology, 45(20), 8858-8865.

Rosén, P., Vogel, H., Cunningham, L., Reuss, N., Conley, D. J., & Persson, P. 2010. Fourier transform infrared spectroscopy, a new method for rapid determination of total organic and inorganic carbon and biogenic silica concentration in lake sediments. Journal of Paleolimnology, 43(2), 247-259.

Rothwell, R. G., & Rack, F. R. 2006. New techniques in sediment core analysis: an introduction. Geological Society, London, Special Publications, 267(1), 1-29.

Russell, J. D., & Fraser, A. R. 1994. Infrared methods. In Clay Mineralogy: Spectroscopic and chemical determinative methods. Springer, Dordrecht. 11-67.

Salomon, F., Goiran, J. P., Noirot, B., Pleuger, E., Bukowiecki, E., Mazzini, I., ... & Germoni, P. (2018). Geoarchaeology of the Roman port-city of Ostia: Fluvio-coastal mobility, urban development and resilience. Earth-Science Reviews, 177, 265-283.

Schulz, B., Sandmann, D., & Gilbricht, S. 2020. SEM-based automated mineralogy and its application in geo-and material sciences. Minerals, 10(11), 1004.

Siebielec, G., McCarty, G. W., Stuczynski, T. I., & Reeves III, J. B. 2004. Near-and mid-infrared diffuse reflectance spectroscopy for measuring soil metal content. Journal of environmental quality, 33(6), 2056-2069.

Solotchina, E. P., Prokopenko, A. A., Kuzmin, M. I., Solotchin, P. A., & Zhdanova, A. N. 2009. Climate signals in sediment mineralogy of Lake Baikal and Lake Hovsgol during the LGM-Holocene transition and the 1-Ma carbonate record from the HDP-04 drill core. Quaternary International, 205(1-2), 38-52.

Sorrel, P., Jacq, K., Van Exem, A., Escarguel, G., Dietre, B., Debret, M., McGowan, S., Ducept, J., Gauthier, E., & Oberhänsli, H. 2021. Evidence for centennial-scale Mid-Holocene episodes of hypolimnetic anoxia in a high-altitude lake system from central Tian Shan (Kyrgyzstan). Quaternary Science Reviews, 252, 106748.

Środoń, J. 2002. Quantitative mineralogy of sedimentary rocks with emphasis on clays and with applications to K-Ar dating. Mineralogical Magazine, 66(5), 677-687.

Styllas, M. 2014. A simple approach to define Holocene sequence stratigraphy using borehole and cone penetration test data. Sedimentology, 61(2), 444-460.

Tamburini, F., Adatte, T., Föllmi, K., Bernasconi, S. M., & Steinmann, P. 2003. Investigating the history of East Asian monsoon and climate during the last glacial–interglacial period (0–140 000 years):

mineralogy and geochemistry of ODP Sites 1143 and 1144, South China Sea. Marine Geology, 201(1-3), 147-168.

Van Exem, A., Debret, M., Copard, Y., Verpoorter, C., De Wet, G., Lecoq, N., Sorrel, P., Werner, A., Roof, S., Laignel, B., & Retelle, M. 2019. New source-to-sink approach in an arctic catchment based on hyperspectral core-logging (Lake Linné, Svalbard). Quaternary Science Reviews, 203, 128-140.

Verpoorter, C., Carrère, V., & Combe, J.-P. 2014. Visible, near-infrared spectrometry for simultaneous assessment of geophysical sediment properties (water and grain size) using the Spectral Derivative-Modified Gaussian Model. Journal of Geophysical Research: Earth Surface, 119(10), 2098–2122. https://doi.org/10.1002/2013JF002969

Viscarra Rossel, R. A., & Behrens, T. 2010. Using data mining to model and interpret soil diffuse reflectance spectra. Geoderma, 158(1–2), 46–54. https://doi.org/10.1016/j.geoderma.2009.12.025

Vogel, H., Meyer-Jacob, C., Thöle, L., Lippold, J. A., & Jaccard, S. L. 2016. Quantification of biogenic silica by means of Fourier transform infrared spectroscopy (FTIRS) in marine sediments. Limnology and oceanography: methods, 14(12), 828-838.

Vogel, H., Rosén, P., Wagner, B., Melles, M., & Persson, P. 2008. Fourier transform infrared spectroscopy, a new cost-effective tool for quantitative analysis of biogeochemical properties in long sediment records. Journal of Paleolimnology, 40(2), 689-702.

Wahab, H. S. A., & Stanley, D. J. 1991. Clay mineralogy and the recent evolution of the north-central Nile delta, Egypt. Journal of Coastal Research, 317-329.

Wan, S., Li, A., Clift, P. D., & Stuut, J. B. W. 2007. Development of the East Asian monsoon: mineralogical and sedimentologic records in the northern South China Sea since 20 Ma. Palaeogeography, Palaeoclimatology, Palaeoecology, 254(3-4), 561-582.

Wang, Y., Fan, D., Liu, J. T., & Chang, Y. 2016. Clay-mineral compositions of sediments in the Gaoping River-Sea system: Implications for weathering, sedimentary routing and carbon cycling. Chemical Geology, 447, 11-26.

Willis, J. P. 1986. Instrumental analytical techniques in geochemistry: Requirements and applications. Fresenius' Zeitschrift für analytische Chemie, 324(8), 855-864.

Wold, S., Ruhe, A., Wold, H., & Dunn, III, W. J. 1984. The Collinearity Problem in Linear Regression. The Partial Least Squares (PLS) Approach to Generalized Inverses. SIAM Journal on Scientific and Statistical Computing, 5(3), 735–743.

Zaeem, M., Nadeem, M., Pham, T. H., Ashiq, W., Ali, W., Gillani, S. S. M., Moise, E. R. D., Leier, H., Kavanagh, V., Galagedara, L., Cheema, M., & Thomas, R. 2021. Development of a hyperspectral imaging technique using LA-ICP-MS to show the spatial distribution of elements in soil cores. Geoderma, 385, 114831.

Zonta, R., Fontolan, G., Cassin, D., & Dominik, J. 2021. X-ray Computed Tomography as a Tool for Screening Sediment Cores: An Application to the Lagoons of the Po River Delta (Italy). Journal of Marine Science and Engineering, 9(3), 323.

Tables

Table 1: Summary of synthetic mixture showing the mineral %wt by sample.

Table 2:Radiocarbon age determination of the ALB-1 core sediments.

Table 3: Correlation matrix of different mineralogical and physical properties of ALB-1 core sediment samples.

Figures captions

Figure 1: Location map of the Albegna fluvial-deltaic environment at different spatial scales. (A) the Albegna watershed limits and relief, (B) the simplified lithological map of the Albegna watershed and its surroundings and (C) the Albegna low-lying area and the current extensions of the Orbetello lagoon.

Figure 2: Schematic demonstration of the research methodology. Step 1: Scanning of the core by SWIR-HSI; Step 2: Measurement of core samples by DRIFTS; Step 3: Conversion of core sample spectra into mineral abundances; Step 4: Combination of SWIR-HSI and DRIFTS spectra over the area sampled for DRIFTS; Step 5: Calibration of SWIR-HSI data to continuous record of mineral abundances along the core.

Figure 3: Chronostratigraphy of the drill core ALB-1. The figure displays: (A) the texture of sediments, (B) the magnetic susceptibility and grain-size analyses, (C) the mineral abundances %wt by sample,

inferred by DRIFT spectroscopy and (D) the high resolution prediction of mineral abundances obtained by the calibrated SWIR-HSI.

Figure 4: Overview spectra obtained from the synthetic mixture samples composed of pure minerals and potassium bromide (KBr). The red line highlights the peaks, selected for the establishment of the calibration curves.

Figure 5: Descriptive statistics of the short-wave spectra (nm units) obtained by the Hyperspectral Imaging and the mid-infrared spectra (cm-1 units) obtained by the Diffuse Reflectance Infrared Fourier Transform Spectroscopy. Grey lines highlight specific absorbance peaks discussed in this study. Statistics were performed on 60 SWIR-HSI and 60 DRIFTS corresponding spectra of sediment samples along the entire ALB-1 core.

Figure 6: Two-dimensional scatter plot of the DRIFT-inferred mineral %wt and the known mineral %wt. The regression line has drowned in black and the confident levels (0.95) in grey. Linear regression equations employed for the mineral %wt estimations are reported.

Figure 7: Two-dimensional scatter plot of PLSR-SWIR predicted mineral %wt and the DRIFT-inferred mineral %wt. The PLSR line is drown in black and the confident levels (0.95) in grey. Raw PLSR coefficients for each modeled mineral are reported. Most discriminant coefficients (peaks) are identified and highlighted.

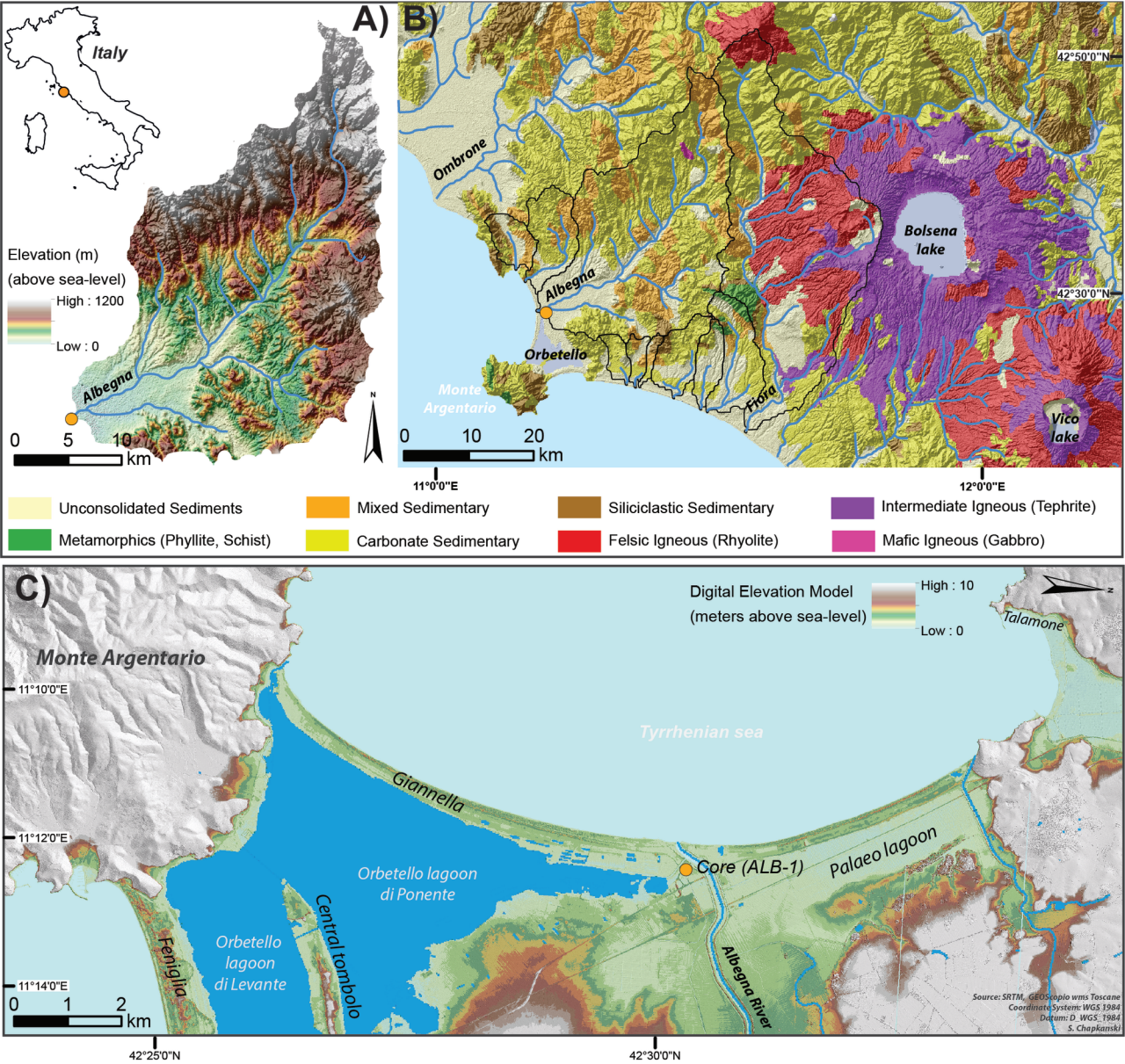
A)
Italy
Elevation (m)
(above sea-level)
High : 1200
Low : 0
Albegna
0 5 10
km
N
B)
42°50'0"N
Ombrone
Bolsena lake
Albegna
42°30'0"N
Orbetello
Monte Argentario
Fiora
Vico lake
0 10 20
km
11°0'0"E
12°0'0"E
Unconsolidated Sediments
Mixed Sedimentary
Siliciclastic Sedimentary
Intermediate Igneous (Tephrite)
Metamorphics (Phyllite, Schist)
Carbonate Sedimentary
Felsic Igneous (Rhyolite)
Mafic Igneous (Gabbro)
C)
Digital Elevation Model
(meters above sea-level)
High : 10
Low : 0
Talamone
Monte Argentario
11°10'0"E
Tyrrhenian sea
Giannella
11°12'0"E
Core (ALB-1)
Palaeo lagoon
Orbetello lagoon di Ponente
Central tombolo
Orbetello lagoon di Levante
Feniglia
Albegna River
11°14'0"E
0 1 2
km
Source: SRTM, GEOScapio wms Toscane
Coordinate System: WGS 1984
Datum: D_WGS_1984
S. Chapkanski
42°25'0"N
42°30'0"N

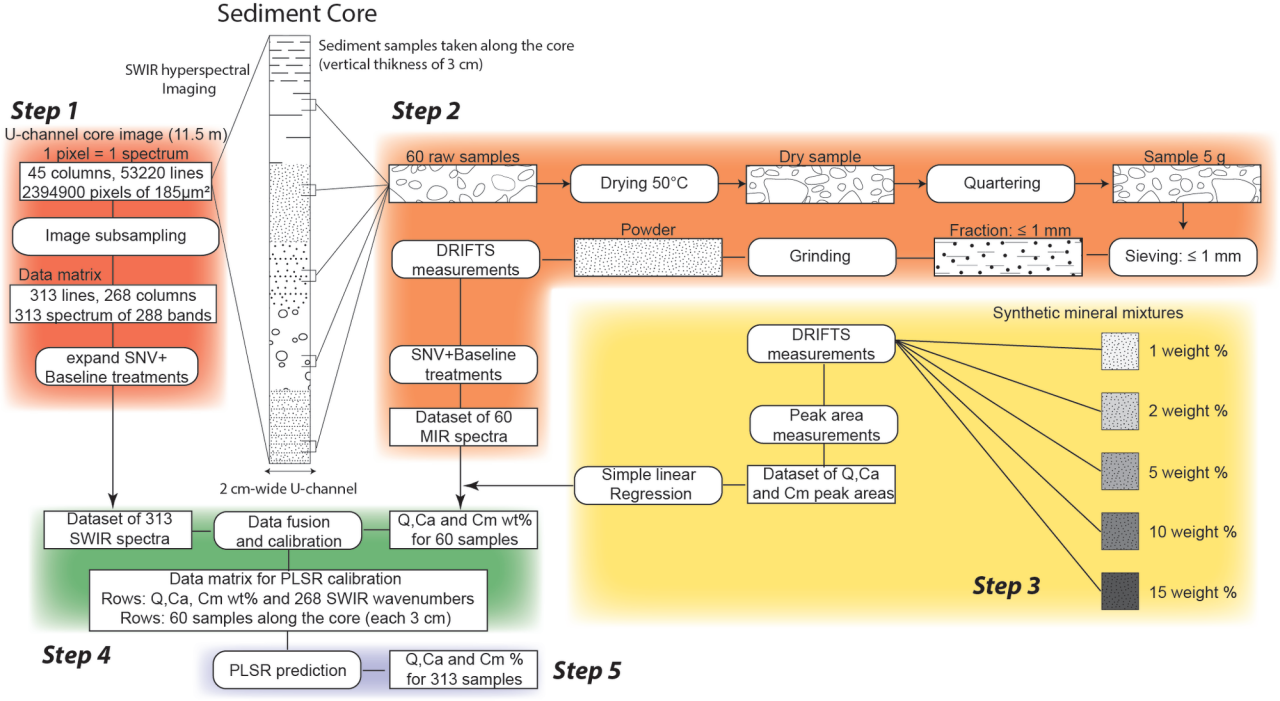
Sediment Core
SWIR hyperspectral Imaging
Sediment samples taken along the core (vertical thikness of 3 cm)
Step 1
U-channel core image (11.5 m)
1 pixel = 1 spectrum
45 columns, 53220 lines
2394900 pixels of 185µm²
Image subsampling
Data matrix
313 lines, 268 columns
313 spectrum of 288 bands
expand SNV+ Baseline treatments
2 cm-wide U-channel
Step 2
60 raw samples
Drying 50°C
Dry sample
Quartering
Sample 5 g
Sieving: ≤ 1 mm
Fraction: ≤ 1 mm
Grinding
Powder
DRIFTS measurements
SNV+Baseline treatments
Dataset of 60 MIR spectra
Synthetic mineral mixtures
DRIFTS measurements
Peak area measurements
Dataset of Q,Ca and Cm peak areas
Simple linear Regression
1 weight %
2 weight %
5 weight %
10 weight %
15 weight %
Step 3
Dataset of 313 SWIR spectra
Data fusion and calibration
Q,Ca and Cm wt% for 60 samples
Data matrix for PLSR calibration
Rows: Q,Ca, Cm wt% and 268 SWIR wavenumbers
Rows: 60 samples along the core (each 3 cm)
Step 4
PLSR prediction
Q,Ca and Cm % for 313 samples
Step 5

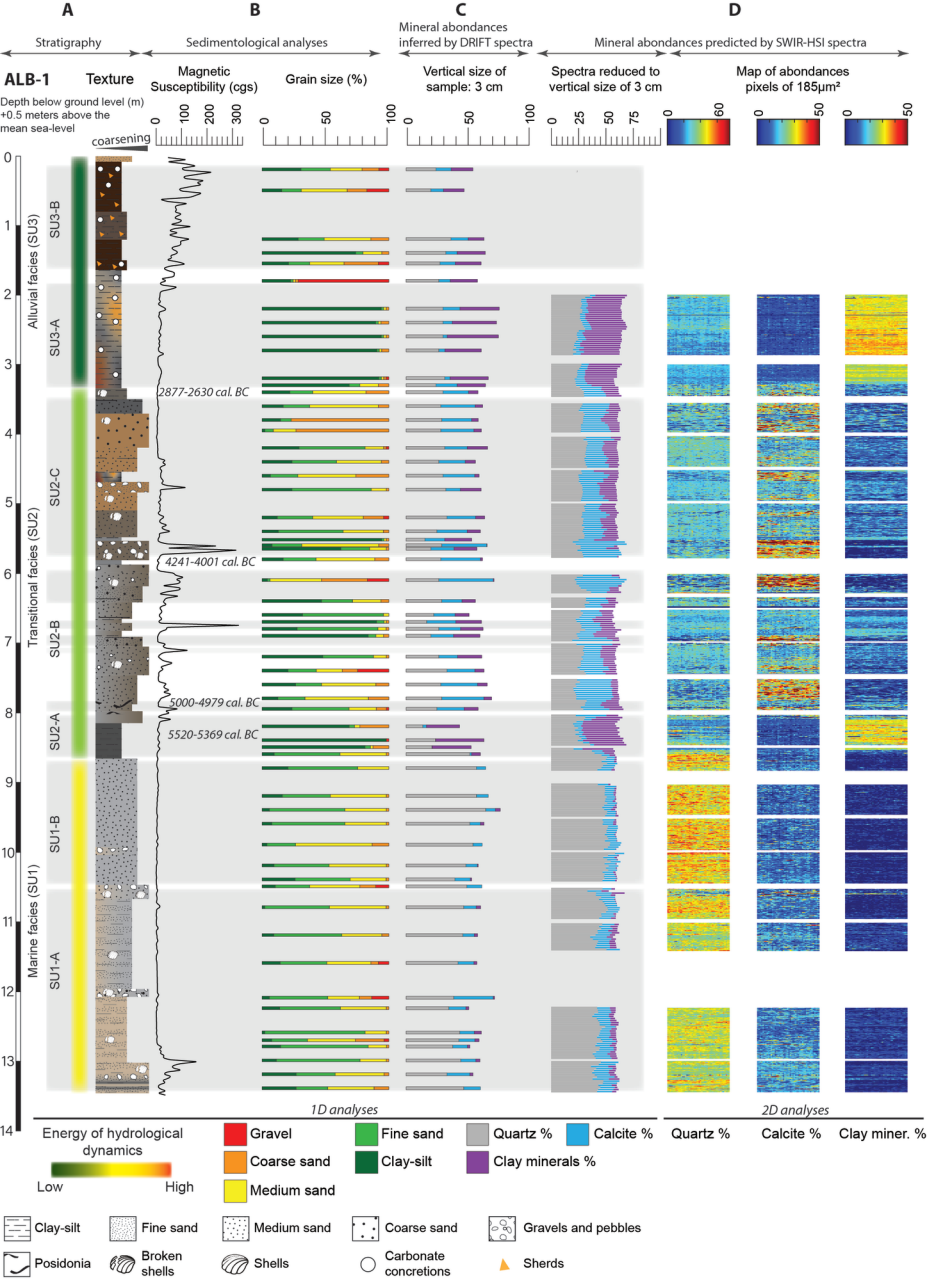
A
B
C
D
Stratigraphy
Sedimentological analyses
Mineral abondances inferred by DRIFT spectra
Mineral abondances predicted by SWIR-HSI spectra
ALB-1
Texture
Magnetic Susceptibility (cgs)
Grain size (%)
Vertical size of sample: 3 cm
Spectra reduced to vertical size of 3 cm
Map of abondances pixels of 185µm²
Depth below ground level (m)
+0.5 meters above the mean sea-level
coarsening
Alluvial facies (SU3)
Transitional facies (SU2)
Marine facies (SU1)
SU3-B
SU3-A
SU2-C
SU2-B
SU2-A
SU1-B
SU1-A
2877-2630 cal. BC
4241-4001 cal. BC
5000-4979 cal. BC
5520-5369 cal. BC
1D analyses
2D analyses
Quartz %
Calcite %
Clay miner. %
Energy of hydrological dynamics
Low
High
Gravel
Coarse sand
Medium sand
Fine sand
Clay-silt
Quartz %
Clay minerals %
Calcite %
Clay-silt
Fine sand
Medium sand
Coarse sand
Gravels and pebbles
Posidonia
Broken shells
Shells
Carbonate concretions
Sherds

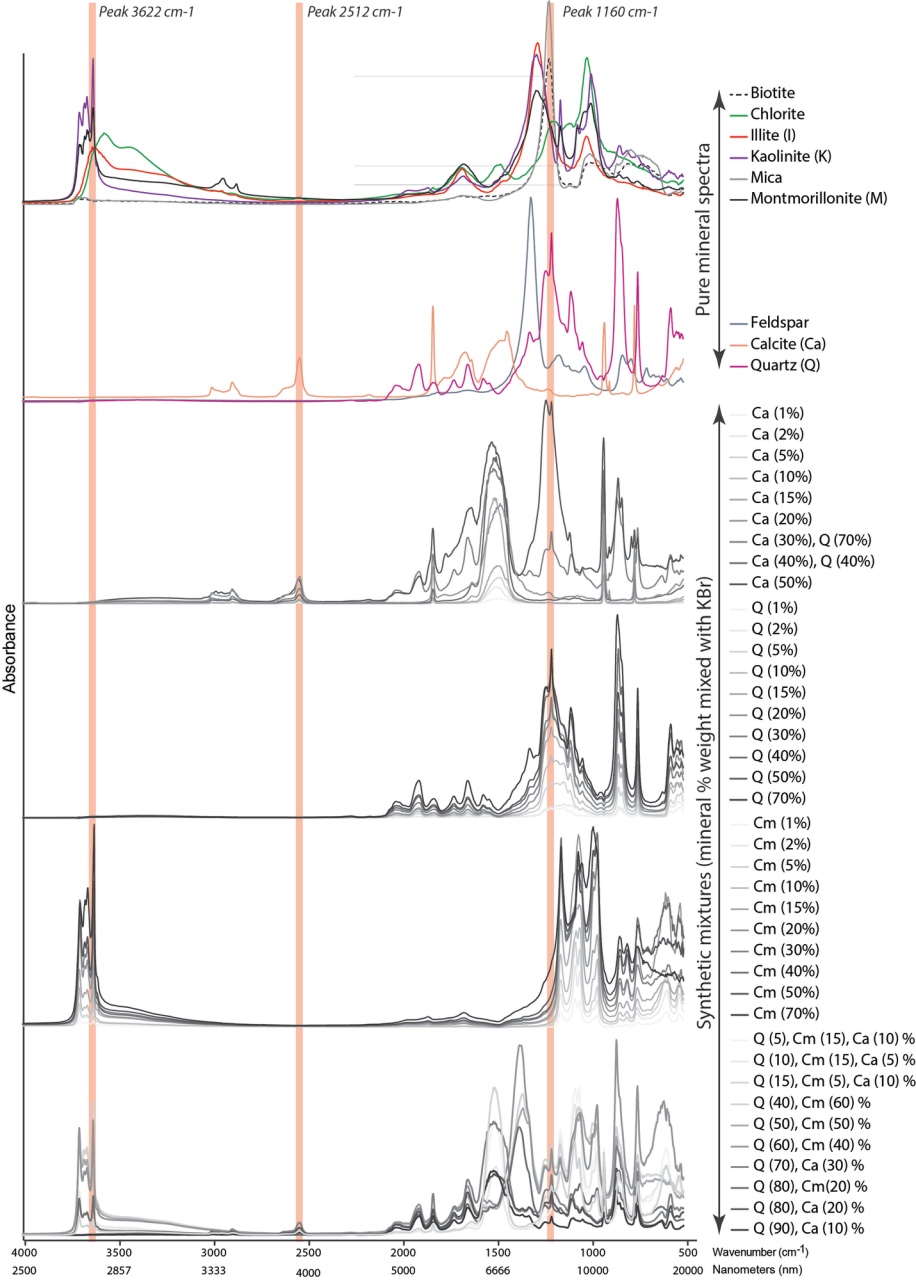
Peak 3622 cm-1
Peak 2512 cm-1
Peak 1160 cm-1
Absorbance
Pure mineral spectra
Biotite
Chlorite
Illite (I)
Kaolinite (K)
Mica
Montmorillonite (M)
Feldspar
Calcite (Ca)
Quartz (Q)
Synthetic mixtures (mineral % weight mixed with KBr)
Ca (1%)
Ca (2%)
Ca (5%)
Ca (10%)
Ca (15%)
Ca (20%)
Ca (30%), Q (70%)
Ca (40%), Q (40%)
Ca (50%)
Q (1%)
Q (2%)
Q (5%)
Q (10%)
Q (15%)
Q (20%)
Q (30%)
Q (40%)
Q (50%)
Q (70%)
Cm (1%)
Cm (2%)
Cm (5%)
Cm (10%)
Cm (15%)
Cm (20%)
Cm (30%)
Cm (40%)
Cm (50%)
Cm (70%)
Q (5), Cm (15), Ca (10) %
Q (10), Cm (15), Ca (5) %
Q (15), Cm (5), Ca (10) %
Q (40), Cm (60) %
Q (50), Cm (50) %
Q (60), Cm (40) %
Q (70), Ca (30) %
Q (80), Cm(20) %
Q (80), Ca (20) %
Q (90), Ca (10) %
4000 3500 3000 2500 2000 1500 1000 500
Wavenumber (cm-1)
2500 2857 3333 4000 5000 6666 10000 20000
Nanometers (nm)

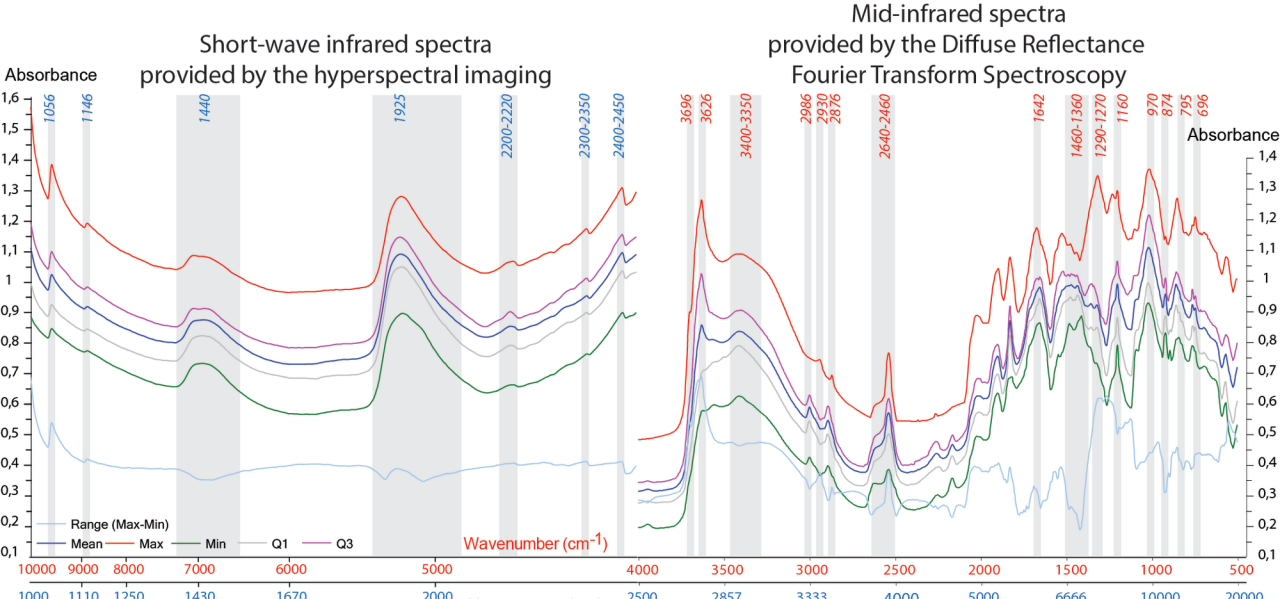
Short-wave infrared spectra
provided by the hyperspectral imaging
Mid-infrared spectra
provided by the Diffuse Reflectance
Fourier Transform Spectroscopy
Absorbance
1056
1146
1440
1925
2200-2220
2300-2350
2400-2450
3696
3626
3400-3350
2986
2930
2876
2640-2460
1642
1460-1360
1290-1270
1160
970
874
795
696
Range (Max-Min)
Mean
Max
Min
Q1
Q3
Wavenumber (cm-1)
Nanometers (nm)

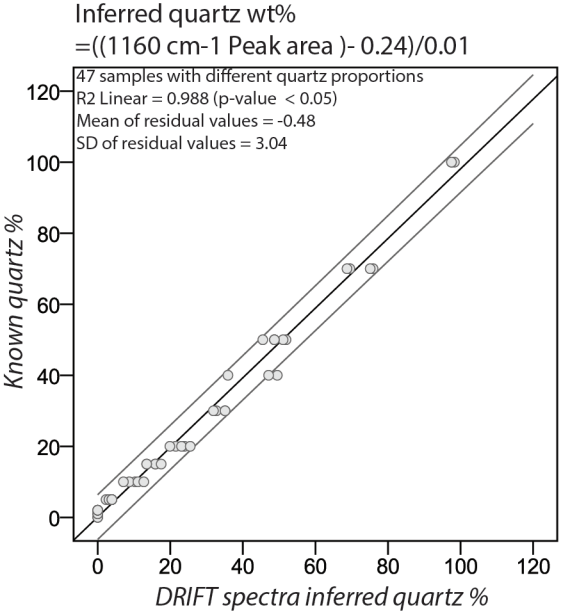
Inferred quartz wt%
=((1160 cm-1 Peak area)- 0.24)/0.01
47 samples with different quartz proportions
R2 Linear = 0.988 (p-value < 0.05)
Mean of residual values = -0.48
SD of residual values = 3.04
Known quartz %
DRIFT spectra inferred quartz %

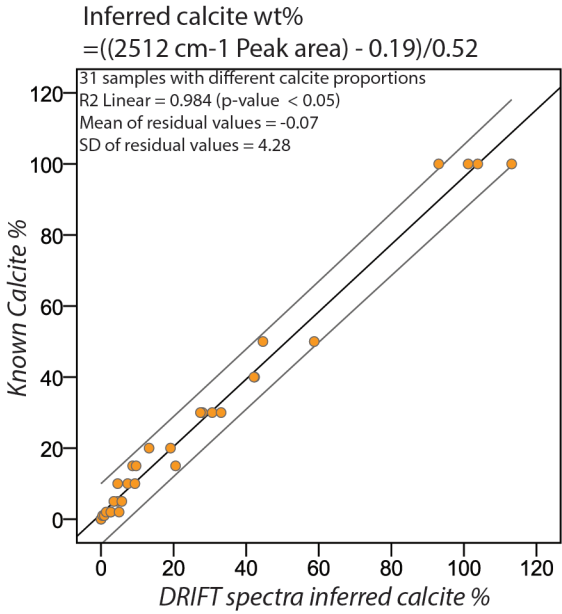
Inferred calcite wt%
=((2512 cm-1 Peak area) - 0.19)/0.52
31 samples with different calcite proportions
R2 Linear = 0.984 (p-value < 0.05)
Mean of residual values = -0.07
SD of residual values = 4.28
Known Calcite %
DRIFT spectra inferred calcite %

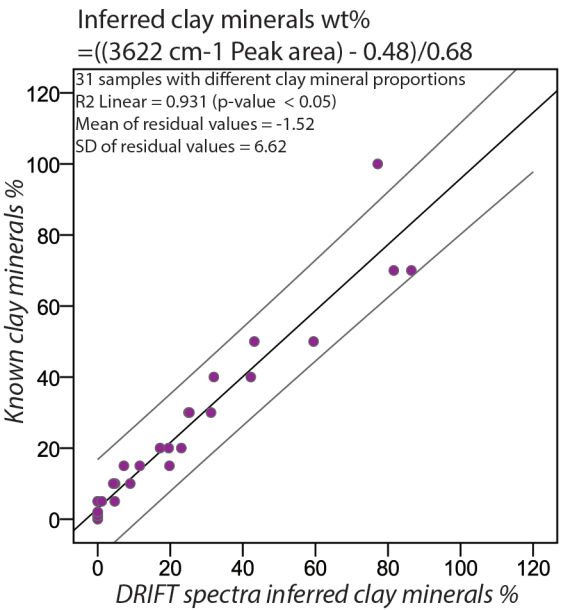
Inferred clay minerals wt%
=((3622 cm-1 Peak area) - 0.48)/0.68
31 samples with different clay mineral proportions
R2 Linear = 0.931 (p-value < 0.05)
Mean of residual values = -1.52
SD of residual values = 6.62
Known clay minerals %
DRIFT spectra inferred clay minerals %

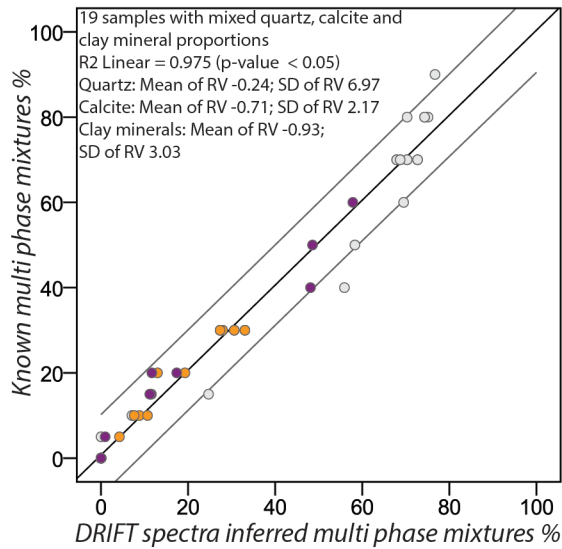
19 samples with mixed quartz, calcite and
clay mineral proportions
R2 Linear = 0.975 (p-value < 0.05)
Quartz: Mean of RV -0.24; SD of RV 6.97
Calcite: Mean of RV -0.71; SD of RV 2.17
Clay minerals: Mean of RV -0.93;
SD of RV 3.03
Known multi phase mixtures %
DRIFT spectra inferred multi phase mixtures %

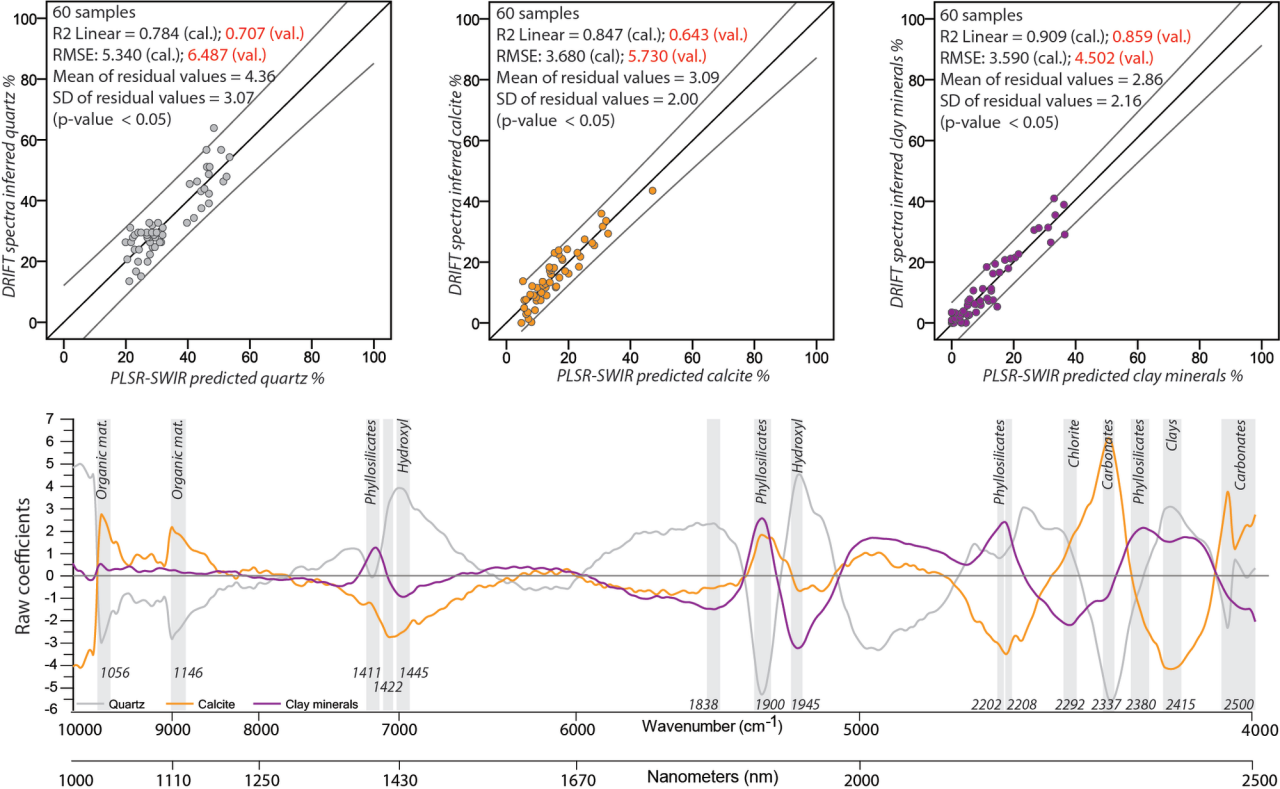
60 samples
R2 Linear = 0.784 (cal.); 0.707 (val.)
RMSE: 5.340 (cal.); 6.487 (val.)
Mean of residual values = 4.36
SD of residual values = 3.07
(p-value < 0.05)
DRIFT spectra inferred quartz %
PLSR-SWIR predicted quartz %
60 samples
R2 Linear = 0.847 (cal.); 0.643 (val.)
RMSE: 3.680 (cal); 5.730 (val.)
Mean of residual values = 3.09
SD of residual values = 2.00
(p-value < 0.05)
DRIFT spectra inferred calcite %
PLSR-SWIR predicted calcite %
60 samples
R2 Linear = 0.909 (cal.); 0.859 (val.)
RMSE: 3.590 (cal.); 4.502 (val.)
Mean of residual values = 2.86
SD of residual values = 2.16
(p-value < 0.05)
DRIFT spectra inferred clay minerals %
PLSR-SWIR predicted clay minerals %
Raw coefficients
Organic mat.
Organic mat.
Phyllosilicates
Hydroxyl
Phyllosilicates
Hydroxyl
Phyllosilicates
Chlorite
Carbonates
Phyllosilicates
Clays
Carbonates
1056
1146
1411
1422
1445
1838
1900
1945
2202
2208
2292
2337
2380
2415
2500
Quartz
Calcite
Clay minerals
Wavenumber (cm-1)
Nanometers (nm)

ID	Quartz wt%	Calcite wt%	KaolMontmIllite (1:1:1) wt%	KBr wt%
Ca1	0	1	0	99
Ca2	0	2	0	98
Ca5	0	5	0	95
Ca10	0	10	0	90
Ca15	0	15	0	85
Ca20	0	20	0	80
Ca50	0	50	0	50
Ca100	0	100	0	0
Cm1	0	0	1	99
Cm2	0	0	2	98
Cm5	0	0	5	95
Cm10	0	0	10	90
Cm15	0	0	15	85
Cm20	0	0	20	80
Cm30	0	0	30	70
Cm40	0	0	40	60
Cm50	0	0	50	50
Cm70	0	0	70	30
Cm100	0	0	100	0
Q1	1	0	0	99
Q2	2	0	0	98
Q5K15Ca10	5	10	15	70
Q5	5	0	0	95
Q10K15Ca5	10	5	15	70
Q10	10	0	0	90
Q15K5Ca10	15	10	5	70
Q15	15	0	0	85
Q20	20	0	0	80
Q20Cm80	20	0	80	0
Q30	30	0	0	70
Q40Cm60	40	0	60	0
Q40	40	0	0	60
Q40Ca40	40	40	0	20
Q50Cm50	50	0	50	0
Q50	50	0	0	50
Q60Cm40	60	0	40	0
Q70Ca30	70	30	0	0
Q70	70	0	0	30
Q80Cm20	80	0	20	0
Q80Ca20	80	20	0	0
Q90Ca10	90	10	0	0
Q100	100	0	0	0

Core	Depth (below soil topographic level)	Stratigraphic Units	Laboratory code	Dating support	14 C age in BP	Age calibrated (Reimer et al., 2020)
ALB-1	349 cm	SU2-C	Lyon-18795	Wood	4155 ± 30	2877 to 2630 BC
ALB-1	597 cm	SU2-C	Lyon-18796	Organic matter	5300 ± 30	4241 to 4001 BC
ALB-1	790-792 cm	SU2-B	Lyon-18797	Charcoal	6015 ± 35	5000 to 4797 BC
ALB-1	823-826 cm	SU2-A	Lyon-18798	Organic matter	6485 ± 35	5520 to 5369 BC

Correlations

DRIFTS inferred quartz (%)	1.00														
DRIFTS inferred calcite (%)	-0.36	1.00													
DRIFTS inferred clay-minerals (%)	-0.58	-0.39	1.00												
PLSR-SWIR predicted quartz (%)	**0.89**	-0.36	**-0.64**	1.00											
PLSR-SWIR predicted calcite (%)	-0.35	**0.92**	-0.37	-0.39	1.00										
PLSR-SWIR predicted clay-minerals (%)	**-0.60**	-0.35	**0.95**	**-0.68**	-0.39	1.00									
Clay-silt texture (%)	-0.56	-0.36	**0.91**	-0.58	-0.37	**0.86**	1.00								
Fine-Sand (%)	0.52	-0.13	-0.52	**0.62**	-0.10	-0.56	**-0.62**	1.00							
Medium-Sand (%)	0.48	0.39	**-0.78**	0.46	0.40	**-0.75**	**-0.74**	0.23	1.00						
Coarse-Sand (%)	-0.16	0.39	-0.18	-0.21	0.37	-0.06	-0.25	-0.37	0.01	1.00					
Total sand (%)	0.57	0.32	**-0.90**	**0.60**	0.34	**-0.86**	**-0.99**	**0.65**	**0.74**	0.23	1.00				
Gravel (%)	0.00	0.27	-0.13	-0.07	0.25	-0.12	-0.15	-0.16	0.06	0.16	0.01	1.00			
Magnetic susceptibility	-0.25	0.37	-0.02	-0.22	0.45	-0.11	-0.03	0.04	0.08	-0.08	0.02	0.09	1.00		
Moisture peak at 1935 nm	0.09	0.13	-0.04	0.06	0.17	-0.10	-0.06	-0.06	0.30	-0.25	0.03	0.24	0.23	1.00	
Hydroxyl bonds peak at 1450 nm	-0.41	-0.18	**0.69**	-0.47	-0.17	**0.68**	**0.73**	**-0.61**	-0.37	-0.20	**-0.74**	-0.01	0.03	0.44	1.00